Transition of responsive mechanosensitive elements from focal adhesions to adherens junctions upon epithelial differentiation

Barbara Noethel*, Lena Ramms*, Georg Dreissen*, Marco Hoffmann*, Ronald Springer*, Matthias Rübsam†, Wolfgang H. Ziegler‡, Carien M. Niessen†, Rudolf Merkel*, Bernd Hoffmann*‖

* Forschungszentrum Jülich, Institute of Complex Systems, ICS-7: Biomechanics, Germany

†Department of Dermatology, Cologne Excellence Cluster on Cellular Stress Responses in Aging-Associated Diseases (CECAD), Center for Molecular Medicine Cologne, University of Cologne, 50931 Cologne, Germany

‡Dept. of Pediatric Kidney, Liver and Metabolic Diseases, Hannover Medical School, Germany

‖ To whom correspondence should be addressed

Dr. Bernd Hoffmann: Institute of Complex Systems, ICS-7

Forschungszentrum Jülich

52425 Jülich, Germany

Tel.: +49 (0)2461 61 6734

Email: b.hoffmann@fz-juelich.de

Running Title: FA/AJ mechanosensitive interplay

Keywords: vinculin, α-catenin, focal adhesion, adherens junction, epidermis, multi-layered epithelia

Abstract

The skin's epidermis is a multi-layered epithelial tissue and the first line of defense against mechanical stress. Its barrier function depends on an integrated assembly and reorganization of cell-matrix and cell-cell junctions in the basal layer and on different intercellular junctions in suprabasal layers. However, how mechanical stress is recognized and which adhesive and cytoskeletal components are involved is poorly understood. Here, we subjected keratinocytes to cyclic stress in the presence or absence of intercellular junctions. Both states not only recognized but also responded to strain by reorienting actin filaments perpendicular to the applied force. Using different keratinocyte mutant strains that altered the mechanical link of the actin cytoskeleton to either cell-matrix or cell-cell junctions, we show that not only focal adhesions but also adherens junctions function as mechanosensitive elements in response to cyclic strain. Loss of paxillin or talin impaired focal adhesion formation and only affected mechanosensitivity in the absence but not presence of intercellular junctions. Further analysis revealed the adherens junction protein α-catenin as a main mechanosensor, with greatest sensitivity conferred upon binding to vinculin. Our data reveal a mechanosensitive transition from cell-matrix to cell-cell adhesions upon formation of keratinocyte monolayers with vinculin and α-catenin as vital players.

(200 words)

Introduction

The epidermal skin barrier is essential to protect the organism from external factors while being permanently affected by mechanical stress (Sanders *et al.*, 1995; Chuong *et al.*, 2002). To ensure tissue integrity and proper barrier function, this self-renewing, multi-layered epithelium dynamically organizes specialized cell-matrix and cell-cell junctions in a layer-dependent fashion (Simpson *et al.*, 2011). With focal adhesions (FAs) cell-matrix adhesions are present in the basal epidermal layer to connect the extracellular basement membrane with the actin cytoskeleton. Furthermore, adherens junctions (AJs) are formed as intercellular contacts. Here, classical cadherins interact through β-catenin and α-catenin (Vasioukhin *et al.*, 2000) to actin (Rudiger, 1998). Initiation of differentiation induces upward movement of keratinocytes into the first suprabasal layer, resulting in loss of FAs while at the same time reorganizing and potentially strengthening AJs (Eckert, 1989; Simpson *et al.*, 2011; Rubsam *et al.*, 2017; Miroshnikova *et al.*, 2018). As cadherins are Ca^{2+}-dependent adhesion molecules, intercellular contact formation and differentiation of epithelia can be mimicked *in vitro* by switching cells to high levels of calcium (O'Keefe *et al.*, 1987; Fuchs, 1990; Vaezi *et al.*, 2002).

Due to permanent exposure of the skin to mechanical stimuli, mechanosensoric proteins perceive the mechanical signal and induce cellular responses within the epidermis to adapt to such impacts. Various mechanisms for mechanosensation have been described. One of them is strain induced conformational changes of proteins leading to exposure of hidden domains (Bakolitsa *et al.*, 2004; Yonemura *et al.*, 2010; Twiss and de Rooij, 2013). For AJs, conformational changes in α-catenin have been shown upon force application (Yonemura *et al.*, 2010; Twiss and de Rooij, 2013; Yao *et al.*, 2014). For FAs several of such proteins have been described, with tension-dependent conformational opening of talin and subsequent binding to integrins and actin mentioned just as example (del Rio *et al.*, 2009).

One vital response to strain is the reorientation of actin bundles within the cell (Hayakawa *et al.*, 2000; Wang *et al.*, 2001; Neidlinger-Wilke *et al.*, 2002). Above a certain threshold in stretch amplitude and frequency, stress fibers reorient away from the direction of strain in order to maintain mechanical homeostasis (Hayakawa *et al.*, 2000; Hayakawa *et al.*, 2001; Wang *et al.*, 2001; Jungbauer *et al.*, 2008). However, until now almost all experiments on cellular strain response have been performed on the single cell level, leading to the identification of mainly FA bound mechnosensoric proteins, e.g. vinculin or p130 Cas (Sawada *et al.*, 2006). In contrast, very little is known on strain-induced cytoskeletal reorientation processes in epithelial monolayers that are connected by cell-cell contacts. Interestingly, vinculin is recruited not only to FAs but also to AJs upon formation (Twiss and de Rooij, 2013). In AJs interaction takes place via direct binding to α-catenin in a tension-dependent manner (Yonemura *et al.*, 2010). This interaction is then thought to locally reorganize actomyosin resulting in junctional

strengthening (Huveneers *et al.*, 2012). Furthermore, upon formation of epithelial cell sheets, FAs reorganize with vinculin largely lost from FAs (Opas *et al.*, 1985; Herman *et al.*, 1986; O'Keefe *et al.*, 1987; Hodivala and Watt, 1994; Braga *et al.*, 2009; Mertz *et al.*, 2013).

Here, we have analyzed and compared the cellular response to cyclic strain of a keratinocyte monolayer in low calcium conditions thus permitting only cell-matrix adhesions with the response of a monolayer of cells allowed to form cell-cell contacts and to initiate early differentiation. Our results reveal the presence of two independent mechanosensitive complexes for actin reorientation; FAs for cells without cell-cell contacts, and AJs as a central mechanoresponsive element in calcium-induced early-stage differentiated epidermal cells. Moreover we provide evidence that together with its binding partner vinculin, α-catenin acts as a mechanosensor in this complex, which upon initiation of intercellular adhesion enables a transition process in which the mechanical control of actin reorganizations is transferred from focal adhesions to adherens junctions.

Materials and Methods

Cell culture

Vinculin and E-cadherin-deficient cells were generated from epidermal, murine keratinocytes as described before (Michels *et al.*, 2009; Mertz *et al.*, 2013; Rubsam *et al.*, 2017). All cells were cultivated under sterile conditions at 32°C and 5% (vol/vol) CO_2 in low calcium (< 0.5 mM) containing DMEM/Ham´s F12 medium (Biochrom, Berlin, Germany) supplemented with 10% FCS Gold (chelex treated) (PAA laboratories, Cölbe, Germany), 1% glutamine (Biochrom, Berlin, Germany), 1% penicillin/streptomycin (Biochrom, Berlin, Germany), 0.18 mM adenin (Sigma, St. Louis, USA), 0.5 µg/ml hydrocortisone (Sigma, St. Louis, USA), 5 µg/ml insulin (Sigma, St. Louis, USA), 10 ng/ml EGF (Sigma, St. Louis, USA), 0.05 µg/µl choleratoxin (Sigma, St. Louis, USA) and 5 µg/ml vitamin C (Sigma, St. Louis, USA).

α-catenin plasmids

For full-length α-catenin expression, αE-catenin was amplified from human cDNA and inserted into a pcDNA3 backbone. A 6-myc tag was amplified from pCS2+MT and inserted c-terminally of the α-catenin sequence. For ΔvinBD α-catenin, human αE-catenin cDNA fragments corresponding to the amino acids 1-200 and 377-906 were amplified and inserted into a pcDNA3 backbone including the c-terminal 6-myc tag.

RNAi experiments

siRNA was incorporated using Fuse-It-siRNA fusogenic liposomes (ibidi, Munich, Germany). $ECad^{Ctrl}$ cells and $Vinc^{KO}$ cells were fused for 12 min with siRNA directed against α-catenin 18 h after seeding of cells on 6 well plates and again 24 h after first fusion. 24 h after second fusion, fused and untreated control cells were used for stretch experiments and determination of knockdown efficiency. Knock-down of paxillin and talin in $Vinc^{Ctrl}$ cells was performed using siRNAs against paxillin and talin 1 and talin 2 (Thermo Scientific, Waltham, USA), respectively. RNA isolation and cDNA generation was performed using RNeasy and QuantiTect reverse transcription Kit (Qiagen, Hilden, Germany) according to the manufacturer's protocols. Afterwards, fusion efficiency was quantified by Real Time PCR. Taq Man assays against α-catenin, paxillin, talin and GAPDH as constitutively expressed marker (Qiagen, Hilden, Germany) were used. For reincorporation of human full-length α-catenin (h-αCat) and ΔvinBD α-catenin, cells were knocked-down for endogenous α-catenin first by using a mouse-specific siRNA (siPOOL5, SiTools biotech, Martinsried, Germany). Four hours after siRNA treatment, α-catenin plasmids (full-length and ΔvinBD α-catenin) were incorporated using Viromer RED (Lipocalyx, Halle (Saale)). siRNA treatment and plasmid incorporation were repeated a second time after 24 h to

guarantee high knockdown of endogenous α-catenin and sufficient expression of incorporated α-catenin versions. After further incubation for 24 h cells were transferred to appropriate substrates for further analysis.

Western blot

Western blot analysis of crude protein extracts was performed according to Waschbüsch et al. 2009. Briefly, cells were harvested and lysed in lysis buffer (RIPA, Sigma, St. Louis, USA) supplemented with protease- and phosphatase-inhibitors (P8340, P0044, P5726, Sigma, St. Louis, USA) for 30 min at 4°C. Protein extracts were heat inactivated, separated using 4-20% SDS PAGE gels (Bio-Rad, Hercules, USA) and blotted to PVDF membranes (Bio-Rad, Hercules, USA). Primary antibodies against tubulin (MAB1864, Merck, Darmstadt, Germany), paxillin (AH00492, Invitrogen, Carlsbad, USA), talin (sc-15336, Santa Cruz Biotechnology, Dallas, USA), α-catenin (C2081, Sigma, St. Louis, USA), c-Myc (M5546, Sigma, St. Louis, USA) and E-cadherin (610182, BD Bioscience, Franklin Lakes, USA) were used and detected by alkaline phosphatase-coupled secondary antibodies directed against rat, rabbit and mouse (Sigma, St. Louis, USA), respectively.

Elastic substrate preparation

Elastic silicone chambers for stretch experiments were prepared and calibrated as described previously (Faust *et al.*, 2011). In order to mimic elasticities of the basement membrane in vivo (Tilleman *et al.*, 2004; Pawlaczyk *et al.*, 2013), elasticities were set to 50 kPa. Chambers were coated with fibronectin (20 µg/ml) in PBS for 1 h at 37°C prior to cell seeding. Since VincKO cells were smaller by 30% on average, cell numbers were adapted to ensure identical conditions during monolayer formation (28000 cells/cm^2 for Vinc^{KO} and Vinc^{KO} αCat^{KD} cells and 21000 cells/cm^2 for all other cell types).

Cell straining

Before initiation of cyclic stretch, cells seeded on elastic chambers were incubated with 1.8 mM Ca^{2+} containing media for 2 h and were kept in high calcium media throughout the experiment. Control cells were kept in low calcium cultivation media (< 0.5 mM Ca^{2+}). A linear stage for simultaneous, uniaxial stretch of six chambers was used for the experiments (adapted from single chamber stretcher previously described in Faust *et al.,* 2011). Cells were stretched for 4 h with 300 mHz and 14%. For focal adhesion analyses, 1.8 mM Ca^{2+} was added to the cells for 2 h, 6 h and 24 h. Control cells were kept in low calcium media.

Immunocytochemistry

Immunocytochemistry experiments were performed as described earlier (Faust *et al.*, 2011). Primary antibodies used were anti-vinculin from mouse (V9131, Sigma, St. Louis, USA), anti-vinculin from rabbit

(700062, Invitrogen, Carlsbad, USA), anti-paxillin from mouse (AH00492, CellSignaling, Cambridge, UK) and anti-E-cadherin from mouse (610182, BD Bioscience, San José, USA). Alexa Fluor 488 anti-rabbit from chicken (A21441, Life Technologies, Carlsbad, USA), Alexa Fluor 488 anti-mouse from chicken (A21200, Life Technologies, Carlsbad, USA), Alexa Fluor 633 anti-rabbit from goat (A21071, Life Technologies, Carlsbad, USA) and Alexa Fluor 633 anti-mouse from goat (A21126, Life Technologies, Carlsbad, USA) were used as secondary antibodies. Actin was stained with Alexa Fluor 546 phalloidin (A22283, Life Technologies, Carlsbad, USA) and Alexa Fluor 488-i phalloidin (U0281, Abnova, Taipei City, Taiwan).

Microscopy

Adhesion proteins were analyzed on a confocal laser scanning microscope (LSM 710, Carl Zeiss, Jena, Germany) with a 40x EC-PlanNeofluar/Ph3/1.3 NA oil immersion objective using appropriate settings for excitation and emission. Images for the analysis of actin fiber orientation were done using a widefield microscope (AxioObserver, Carl Zeiss, Jena, Germany) equipped with a 40x EC-PlanNeofluar/Ph3/1.3 NA oil immersion objective (Carl Zeiss, Jena, Germany).

Analysis of actin fiber orientation

The analysis of actin fiber orientation was based on the structure tensor approach described in Faust *et al.* 2011. Here, we manually marked individual cells and excluded the thick fibers encircling the cell. In the inner area, local fiber orientations were determined from gray value gradients. Main actin fiber orientation was determined as the maximum of the distribution of angles within the cell area (parabola fit for suppression of noise).

Detection of focal adhesions

To detect FAs, cells were manually separated on images stained for paxillin. Subsequently, an algorithm described in Hersch *et al.* was used (Hersch *et al.*, 2013). In brief, images were bandpass-filtered (9x9 binomial filter and 45x45 binomial filter subtracted; pixel size 94 nm). Average and standard deviation were determined for each pixel in a 45 pixel wide square centered on it. Pixels with z-score (difference of pixel value and local mean divided by local standard deviation) exceeding one were chosen as candidates. Only connected regions of sizes between 45 and 1000 pixels were considered. FAs with low contrast to their neighborhood were rejected.

Co-Localization analysis

For this analysis, whole images of paxillin and vinculin staining were used. As a pre-processing step, the images were Gaussian filtered (2-D Gaussian smoothing kernel with standard deviation of 0.5, pixel

size 94 nm). Then FAs were detected in both channels as described above and overlapping FA areas in the paxillin and vinculin images were determined.

Determination of actin localization parameter

In a first step, all analyzed actin-labeled cells were marked manually. Then each marked cell was transformed to the unit circle with a radius of 200 pixel as described in Mohl *et al.* (Mohl *et al.*, 2012). This unit cell was subdivided into evenly spaced concentric rings, all with a width of five pixel followed by average gray value calculation for each ring. Then a straight line was fitted to the average gray values. The actin localization parameter was defined as the slope of this line. Positive values indicate high actin concentration in the cellular periphery compared to its center and vice versa.

Statistical analysis

Wilcoxon test was used for determination of statistical significance (upper limits: *P=0.05; **P=0.01; ***P=0.005). Detailed statistical information for all experiments are given in Supplementary Figure 1.

Results

Intercellular contacts reinforce strain-induced stress fiber reorientation

To address whether initiation of intercellular contact formation and differentiation would affect cytoskeletal reorientation in response to cyclic stretch, keratinocyte monolayers were either allowed (high calcium) or not allowed (low calcium) to initiate intercellular junction formation for 2 hours and then subjected to cyclic stretch for 4 hours under the same calcium conditions, and compared to unstretched control cells (Figure 1). Quantitative orientation analyses of actin stress fibers revealed a significant difference between cells that were cyclically stretched in the presence of calcium and those that were kept in low calcium media (Figure 1 E). In both experiments, stress fibers oriented away from the direction of stretch, albeit more extensively in high calcium media, with almost all fibers being in a range between 30°-90° with low calcium and 60°-90° with high calcium. Thus, cells allowed to form intercellular contacts reinforce external stress-induced reorientation of the actin cytoskeleton.

Strain enhances FA loss in epithelial sheets

Based on positive control analyses for the experimental setup according to Twiss and de Rooij (2013) we were also able to detect the switch of vinculin from FAs to AJs, slightly reduced numbers of FAs and actin cytoskeletal cortical ring formation in the presence of 6 h of Ca^{2+} (Supplementary Figure 2). We next tested whether cyclic strain would affect vinculin, paxillin and F-actin localization under high calcium. Applying external force decreased cell coverage of paxillin labeled FAs significantly by more than 65% (Figure 2 A, B). These remaining FAs furthermore slightly decreased in size, while stretch in low calcium had no significant effect (Figure 2 C). In contrast, vinculin incorporation into cell-cell contacts in high calcium medium remained unaffected by cyclic strain. These vinculin-positive structures were not co-stained with the FA marker paxillin, suggesting that AJs also form under cyclic stretch conditions. Furthermore, in contrast to predominantly cortical F-actin in the absence of stretch in high calcium, stretch induced formation of prominent, highly parallelized stress fibers that spanned the whole cell ending at cell-cell contacts on both ends. These F-actin fibers additionally showed a stronger perpendicular reorientation compared to those stretched in low calcium (Figure 2 A, see also Supplementary Figure 2 E).

FAs are largely dispensable for mechanosensation after cell-cell contact formation

Based on our observation of enhanced actin reorientation in response to strain for early cell sheets, we hypothesized that a further mechanosensitive machinery engaged upon cell-cell contact formation.

To investigate this, we impaired the FA-dependent mechanosensitive machinery using vinculin deficient keratinocytes ($Vinc^{KO}$) for stretch experiments (Rubsam *et al.*, 2017). Actin filament orientations were equally distributed in the absence of strain in both control and $Vinc^{KO}$ cells cultured in low calcium (Figure 3 A-C). In contrast, upon stretching in low-calcium media, stress fiber reorientation in $Vinc^{KO}$ cells was strongly reduced, indicating impaired FA-dependent mechanosensitivity (Figure 3 A, D). Under high calcium conditions however, strain-induced actin reorientation was largely restored in $Vinc^{KO}$ cells to almost $Vinc^{Ctrl}$ levels (Figure 3 A, E). Restored reorientation took place only after cell-sheet formation, while high Ca^{2+} conditions on single cell level were unable to improve the impaired reorientation behavior of $Vinc^{KO}$ cells (Supplementary Figure 3). To confirm that the loss of vinculin indeed impaired stress-induced actin reorientaton through FAs, we knocked-down the highly specific FA proteins paxillin and talin, respectively. mRNA levels were decreased to 40%, (s.d. 6%) for paxillin and 10% (s.d. 10%) for talin 1/2 respectively (for protein knock-down efficiency see Supplementary Figure 4). Similar to loss of vinculin, knock-down of paxillin induced a strongly impaired reorientation behavior in the absence of calcium, but had no defect in stress-induced actin reorientation upon calcium-induced AJ formation when compared to WT (Figure 4 A-C). Even more dramatic effects were found after knock-down of talin. Whereas talin-knock-down cells grown in low calcium were still able to adhere weakly in the absence of strain, these cells immediately lost contact upon straining, accompanied by a complete loss of detectable actin bundles. In contrast, high Ca^{2+} restored their ability to respond to strain by forming cell-spanning stress fibers with reorientation angles similar to those of control cells (Figure 4 A, D, E).

Cell-cell contacts are responsible for enhanced fiber reorientation

We next directly addressed how AJs affect force-induced mechanosensation. We first used E-cadherin-deficient ($ECad^{KO}$) keratinocytes (Tunggal *et al.*, 2005), as this is the most abundant classical cadherin in these cells (Michels *et al.*, 2009). However, loss of E-cadherin did not obviously affect the stretch-induced F-actin reorientation response, regardless whether these cells were allowed to form cell-cell junctions (high calcium) or not (low calcium) (Supplementary Figure 5).

Since P-Cadherin is upregulated in the absence of E-Cadherin (Tunggal *et al.*, 2005; Tinkle *et al.*, 2008; Michels *et al.*, 2009) and Supplementary Figure 6), we next used $ECad^{KO}$ keratinocytes additionally knocked down for P-cadherin ($ECad^{KO}PCad^{KD}$, Michels *et al.,* 2009), which lack any detectable classical cadherins (Supplementary Figure 4 A). Under low calcium conditions, $ECad^{KO}PCad^{KD}$ responded similarly to strain as control keratinocytes, in agreement with our observation that FAs are the predominant mechanosensing element under these conditions. However, upon allowing cells to form

intercellular junctions for 6 hours in high calcium, the reinforced actin reorientation seen in control cells is lost and the response remains identical to cells in low calcium conditions (Figure 5 A-C). Together, these data indicate that loss of AJs, impairs early cell-sheet specific mechanosensitivity with FAs as the only functional mechanosensing structure and a response as seen for separated cells.

α-catenin is essential for the mechanosensoric function of AJs

We next asked how AJs control external force-induced cytoskeletal reorientation. As the actin binding protein α-catenin was already identified as force-sensitive protein in AJs (Yonemura *et al.*, 2010) we used siRNA to efficiently knock down α-catenin (mRNA knockdown 87%, (s.d. 6%) (for protein knock-down efficiency see Supplementary Figure 4) in primary control mouse keratinocytes (αCat^{KD}). Knock down of α-catenin strongly reduced the stretch-induced actin reorientation for cells grown in high calcium, which was now almost identical to cells under low calcium conditions or single cells, strongly indicating that upon loss of α-catenin high calcium grown keratinocytes keep using FAs as the main mechanosensitive element in these cells (Figure 5 D-F). Thus, α-catenin is a central mechanosensor of external force in AJs to drive actin reorganization.

Since α-catenin is also necessary to recruit vinculin to AJs in high calcium (Yonemura *et al.*, 2010; Twiss and de Rooij, 2013; Yao *et al.*, 2014), we further investigated whether α-catenin cooperated with vinculin to reorganize actin. For this purpose we used mouse αCat^{KD} cells and re-expressed human full-length α-catenin as well as an α-catenin mutant lacking the vinculin binding domain (ΔvinBD). While all genetic variants responded similarly as control cells to external force at low calcium (Fig. 6 A), formation of AJs at high calcium restored stress-induced actin reorganization in cells expressing human WT α-catenin. In contrast, expression of ΔvinBD α-catenin only partially restored actin reorientation (Figure 6A), thus indicating that α-catenin controls this response in part through vinculin.

Finally, we asked how impairing FA- and AJ-dependent mechanosensitivity would affect F-actin reorganization by knocking down α-catenin in $Vinc^{KO}$ cells ($Vinc^{KO}\alpha Cat^{KD}$). Here, reduced levels of α-catenin had no further effect in low calcium due to the fully FA-dependent mechanosensitivity for these conditions. In contrast, when cells were allowed to induce intercellular junction formation in high calcium we detected a strongly reduced actin reorientation in $Vinc^{KO}\alpha Cat^{K}$ cells compared to $Vinc^{KO}$ cells only. (Figure 6 B). Taken together, our data identify an essential role for FAs and AJs in force-dependent cytoskeletal organization and redistribution and show that both vinculin and α-catenin are essential mechanosensors in keratinocytes.

Discussion

Mechanosensation for FAs as well as AJs depends on their structural ability to bind to actin bundles (Zaidel-Bar *et al.*, 2007; Kanchanawong *et al.*, 2010; Yonemura *et al.*, 2010; Twiss and de Rooij, 2013). While cell spanning actin bundles are present on single cell level in the absence and presence of strain, calcium-induced cell sheet formation leads to enhanced cortical actin localization and significant reduction of stress fibers (see also Supplementary Figure 3). Interestingly, cyclic strain dramatically induces cell spanning stress fiber formation even in cell sheets. Stress induced actin bundles in cell sheets furthermore reorient almost perpendicular to strain direction and are additionally characterized by high order and reduced angular spread. Here, most likely cell cooperativity plays an important role since AJs connect filaments between cells, leading to interdependencies of cytoskeletal orders within cell sheets (Lampugnani, 2010; Millan *et al.*, 2010) . The reason for intense stress fiber formation in cell sheets remains elusive but indicates that strain parameters used here exceed certain thresholds that already have be identified on single cell level (Chien, 2007). Furthermore, why stress fibers reorient to even higher angles in cell sheets than described for single cells (Faust *et al.*, 2011) is unclear.

As part of FA mechanosensitivity, manifold functions are described for vinculin (Carisey *et al.*, 2013; Case *et al.*, 2015) and largely depend on its ability to interact with various binding partners (Geiger and Bershadsky, 2001; Bakolitsa *et al.*, 2004; Ziegler *et al.*, 2006; Case *et al.*, 2015). However, vinculin is not the only molecule in FAs that affects stretch-induced F-actin reorganization, since paxillin or talin knock-down also had similar effects here, which argues for considerable changes in FA composition, maturation or mechanosensitive force sensitivity in these cells (Humphries *et al.*, 2007). Interestingly, formation of AJs largely rescued loss of FA-dependent mechanosensitivity. Although various other types of cell-cell contacts are also present in epithelia, our data indicate the specific loss of mechanosensitivity for $ECad^{KO}PCad^{KD}$ cells. Both classical cadherins seem to complement each other regarding formation of mechanosensitive complexes as shown here for cells deleted for E-cadherin only. Our results fit well to other E-cadherin functions complemented by P-cadherin (Michels et al., 2009).

On the molecular level we showed that AJ-dependent mechanosensitivity is largely dependent on α-catenin as a mechanosensor with loss of cell-sheet specific responsiveness in the absence of α-catenin. The results fit well to data from other groups having described α-catenin as an important force-responsive molecule (Yonemura *et al.*, 2010; Twiss and de Rooij, 2013; Yao *et al.*, 2014). Interestingly, our data indicate that also its binding partner vinculin is important for AJ-dependent mechanosensitivity. These results are supported by magnetic twisting experiments showing that vinculin potentiates the E-cadherin mechanosensory response (le Duc *et al.*, 2010). Since AJ maturation

additionally largely depends on applied forces (Huveneers *et al.*, 2012) and force-induced conformational unfolding of α-catenin allows vinculin binding in a 1:1 ratio (Yao *et al.*, 2014), mechanosensitive cooperativity of α-catenin and vinculin might be due to their ability to both bind to actin filaments.

In our experiments, we were not able to detect intensity differences for AJ-specific vinculin upon strain application, although strain-induced incorporation of vinculin into cell-cell contacts had been described already (Thomas *et al.*, 2013). However, while detecting vinculin in high calcium at every cell-cell border in the absence of strain, we detected vinculin-comprising AJs upon strain application preferentially at ends of reoriented stress fibers and therefore unequally distributed, which agrees well to the hypothesis of vinculin incorporation into active, force bearing AJs (Yonemura *et al.*, 2010).

In summary, our experiments indicate that a functional mechanoperception exists in adhesive cells, no matter if such cell is separated or part of an interconnected cell sheet (see model: Figure 7 and Supplementary Movie 1-4). For epithelial cells, due to disassembly of FAs in suprabasal epithelial cell layers, mechanosensitivity translocates to newly-formed AJs as further force bearing structure. Ultimately in response to stretch, FA as well as AJ-dependent mechanosensitivity induces reorientation of actin bundles away from applied stretch and causes cytoskeletal reinforcement bound to the respective adhesion complexes.

Acknowledgment

This work received funding from the European Union's Horizon 2020 research and innovation programme under the Marie Sklodowska-Curie grant agreement No 642866. It was also supported by the Deutsche Forschungsgemeinschaft (Schwerpunktprogramm SPP1782).

Literature

Bakolitsa, C., Cohen, D.M., Bankston, L.A., Bobkov, A.A., Cadwell, G.W., Jennings, L., Critchley, D.R., Craig, S.W., and Liddington, R.C. (2004). Structural basis for vinculin activation at sites of cell adhesion. Nature *430*, 583-586.

Braga, V.M.M., Hodivala, K.J., and Watt, F.M. (2009). Calcium-Induced Changes in Distribution and Solubility of Cadherins, Integrins and Their Associated Cytoplasmic Proteins in Human Keratinocytes. Cell Commun Adhes *3*, 201-215.

Carisey, A., Tsang, R., Greiner, A.M., Nijenhuis, N., Heath, N., Nazgiewicz, A., Kemkemer, R., Derby, B., Spatz, J., and Ballestrem, C. (2013). Vinculin regulates the recruitment and release of core focal adhesion proteins in a force-dependent manner. Curr Biol *23*, 271-281.

Case, L.B., Baird, M.A., Shtengel, G., Campbell, S.L., Hess, H.F., Davidson, M.W., and Waterman, C.M. (2015). Molecular mechanism of vinculin activation and nanoscale spatial organization in focal adhesions. Nat Cell Biol *17*, 880-892.

Chien, S. (2007). Mechanotransduction and endothelial cell homeostasis: the wisdom of the cell. Am J Physiol Heart Circ Physiol *292*, H1209-1224.

Chuong, C.M., Nickoloff, B.J., Elias, P.M., Goldsmith, L.A., Macher, E., Maderson, P.A., Sundberg, J.P., Tagami, H., Plonka, P.M., Thestrup-Pedersen, K., Bernard, B.A., Schröder, J.M., Dotto, P., Chang, C.H., Williams, M.L., Feingold, K.R., King, L.E., Kligman, A.M., Rees, J.L., and Christophers, E. (2002). What is the 'true' function of skin? Exp Dermatol *11*, 159-187.

del Rio, A., Perez-Jimenez, R., Liu, R., Roca-Cusachs, P., Fernandez, J.M., and Sheetz, M.P. (2009). Stretching single talin rod molecules activates vinculin binding. Science *323*, 638-641.

Eckert, R.L. (1989). Structure, function, and differentiation of the keratinocyte. Physiol Rev *69*, 1316-1346.

Faust, U., Hampe, N., Rubner, W., Kirchgessner, N., Safran, S., Hoffmann, B., and Merkel, R. (2011). Cyclic stress at mHz frequencies aligns fibroblasts in direction of zero strain. PLoS One *6*, e28963.

Fuchs, E. (1990). Epidermal differentiation: the bare essentials. J Cell Biol *111*, 2807-2814.

Geiger, B., and Bershadsky, A. (2001). Assembly and mechanosensory function of focal contacts. Curr Opin Cell Biol *13*, 584-592.

Hayakawa, K., Hosokawa, A., Yabusaki, K., and Obinata, T. (2000). Orientation of Smooth Muscle-Derived A10 Cells in Culture by Cyclic Stretching: Relationship between Stress Fiber Rearrangement and Cell Reorientation. Zoolog Sci *17*, 617-624.

Hayakawa, K., Sato, N., and Obinata, T. (2001). Dynamic reorientation of cultured cells and stress fibers under mechanical stress from periodic stretching. Exp Cell Res *268*, 104-114.

Herman, B., Harrington, M.A., Olashaw, N.E., and Pledger, W.J. (1986). Identification of the cellular mechanisms responsible for platelet-derived growth factor induced alterations in cytoplasmic vinculin distribution. J Cell Physiol *126*, 115-125.

Hersch, N., Wolters, B., Dreissen, G., Springer, R., Kirchgessner, N., Merkel, R., and Hoffmann, B. (2013). The constant beat: cardiomyocytes adapt their forces by equal contraction upon environmental stiffening. Biol Open *2*, 351-361.

Hodivala, K.J., and Watt, F.M. (1994). Evidence that cadherins play a role in the downregulation of integrin expression that occurs during keratinocyte terminal differentiation. J Cell Biol *124*, 589-600.

Humphries, J.D., Wang, P., Streuli, C., Geiger, B., Humphries, M.J., and Ballestrem, C. (2007). Vinculin controls focal adhesion formation by direct interactions with talin and actin. J Cell Biol *179*, 1043-1057.

Huveneers, S., Oldenburg, J., Spanjaard, E., van der Krogt, G., Grigoriev, I., Akhmanova, A., Rehmann, H., and de Rooij, J. (2012). Vinculin associates with endothelial VE-cadherin junctions to control force-dependent remodeling. J Cell Biol *196*, 641-652.

Jungbauer, S., Gao, H., Spatz, J.P., and Kemkemer, R. (2008). Two characteristic regimes in frequency-dependent dynamic reorientation of fibroblasts on cyclically stretched substrates. Biophys J *95*, 3470-3478.

Kanchanawong, P., Shtengel, G., Pasapera, A.M., Ramko, E.B., Davidson, M.W., Hess, H.F., and Waterman, C.M. (2010). Nanoscale architecture of integrin-based cell adhesions. Nature *468*, 580-584.

Lampugnani, M.G. (2010). Endothelial adherens junctions and the actin cytoskeleton: an 'infinity net'? J Biol *9*, 16.
le Duc, Q., Shi, Q., Blonk, I., Sonnenberg, A., Wang, N., Leckband, D., and de Rooij, J. (2010). Vinculin potentiates E-cadherin mechanosensing and is recruited to actin-anchored sites within adherens junctions in a myosin II-dependent manner. J Cell Biol *189*, 1107-1115.
Mertz, A.F., Che, Y., Banerjee, S., Goldstein, J.M., Rosowski, K.A., Revilla, S.F., Niessen, C.M., Marchetti, M.C., Dufresne, E.R., and Horsley, V. (2013). Cadherin-based intercellular adhesions organize epithelial cell-matrix traction forces. Proc Natl Acad Sci U S A *110*, 842-847.
Michels, C., Buchta, T., Bloch, W., Krieg, T., and Niessen, C.M. (2009). Classical Cadherins Regulate Desmosome Formation. Journal of Investigative Dermatology *129*, 2072-2075.
Millan, J., Cain, R.J., Reglero-Real, N., Bigarella, C., Marcos-Ramiro, B., Fernandez-Martin, L., Correas, I., and Ridley, A.J. (2010). Adherens junctions connect stress fibres between adjacent endothelial cells. BMC Biol *8*, 11.
Miroshnikova, Y.A., Le, H.Q., Schneider, D., Thalheim, T., Rubsam, M., Bremicker, N., Polleux, J., Kamprad, N., Tarantola, M., Wang, I., Balland, M., Niessen, C.M., Galle, J., and Wickstrom, S.A. (2018). Adhesion forces and cortical tension couple cell proliferation and differentiation to drive epidermal stratification. Nat Cell Biol *20*, 69-80.
Mohl, C., Kirchgessner, N., Schafer, C., Hoffmann, B., and Merkel, R. (2012). Quantitative mapping of averaged focal adhesion dynamics in migrating cells by shape normalization. J Cell Sci *125*, 155-165.
Neidlinger-Wilke, C., Grood, E., Claes, L., and Brand, R. (2002). Fibroblast orientation to stretch begins within three hours. J Orthop Res *20*, 953-956.
O'Keefe, E.J., Briggaman, R.A., and Herman, B. (1987). Calcium-induced assembly of adherens junctions in keratinocytes. J Cell Biol *105*, 807-817.
Opas, M., Turksen, K., and Kalnins, V.I. (1985). Adhesiveness and distribution of vinculin and spectrin in retinal pigmented epithelial cells during growth and differentiation in vitro. Dev Biol *107*, 269-280.
Pawlaczyk, M., Lelonkiewicz, M., and Wieczorowski, M. (2013). Age-dependent biomechanical properties of the skin. Advances in Dermatology and Allergology/Postępy Dermatologii i Alergologii *30*, 302-306.
Rubsam, M., Mertz, A.F., Kubo, A., Marg, S., Jungst, C., Goranci-Buzhala, G., Schauss, A.C., Horsley, V., Dufresne, E.R., Moser, M., Ziegler, W., Amagai, M., Wickstrom, S.A., and Niessen, C.M. (2017). E-cadherin integrates mechanotransduction and EGFR signaling to control junctional tissue polarization and tight junction positioning. Nat Commun *8*, 1250.
Rudiger, M. (1998). Vinculin and alpha-catenin: shared and unique functions in adherens junctions. Bioessays *20*, 733-740.
Sanders, J.E., Goldstein, B.S., and Leotta, D.F. (1995). Skin-Response to Mechanical-Stress - Adaptation Rather Than Breakdown - a Review of the Literature. Journal of Rehabilitation Research and Development *32*, 214-226.
Sawada, Y., Tamada, M., Dubin-Thaler, B.J., Cherniavskaya, O., Sakai, R., Tanaka, S., and Sheetz, M.P. (2006). Force sensing by mechanical extension of the Src family kinase substrate p130Cas. Cell *127*, 1015-1026.
Simpson, C.L., Patel, D.M., and Green, K.J. (2011). Deconstructing the skin: cytoarchitectural determinants of epidermal morphogenesis. Nat Rev Mol Cell Biol *12*, 565-580.
Thomas, W.A., Boscher, C., Chu, Y.S., Cuvelier, D., Martinez-Rico, C., Seddiki, R., Heysch, J., Ladoux, B., Thiery, J.P., Mege, R.M., and Dufour, S. (2013). alpha-Catenin and vinculin cooperate to promote high E-cadherin-based adhesion strength. J Biol Chem *288*, 4957-4969.
Tilleman, T.R., Tilleman, M.M., and Neumann, M.H. (2004). The elastic properties of cancerous skin: Poisson's ratio and Young's modulus. Isr Med Assoc J. *6*, 753-755.
Tinkle, C.L., Pasolli, H.A., Stokes, N., and Fuchs, E. (2008). New insights into cadherin function in epidermal sheet formation and maintenance of tissue integrity. Proc Natl Acad Sci U S A *105*, 15405-15410.

Tunggal, J.A., Helfrich, I., Schmitz, A., Schwarz, H., Gunzel, D., Fromm, M., Kemler, R., Krieg, T., and Niessen, C.M. (2005). E-cadherin is essential for in vivo epidermal barrier function by regulating tight junctions. EMBO J *24*, 1146-1156.
Twiss, F., and de Rooij, J. (2013). Cadherin mechanotransduction in tissue remodeling. Cell Mol Life Sci *70*, 4101-4116.
Vaezi, A., Bauer, C., Vasioukhin, V., and Fuchs, E. (2002). Actin cable dynamics and Rho/Rock orchestrate a polarized cytoskeletal architecture in the early steps of assembling a stratified epithelium. Dev Cell *3*, 367-381.
Vasioukhin, V., Bauer, C., Yin, M., and Fuchs, E. (2000). Directed Actin Polymerization Is the Driving Force for Epithelial Cell–Cell Adhesion. Cell *100*, 209-219.
Wang, J.H., Goldschmidt-Clermont, P., Wille, J., and Yin, F.C. (2001). Specificity of endothelial cell reorientation in response to cyclic mechanical stretching. J Biomech *34*, 1563-1572.
Yao, M., Qiu, W., Liu, R., Efremov, A.K., Cong, P., Seddiki, R., Payre, M., Lim, C.T., Ladoux, B., Mege, R.M., and Yan, J. (2014). Force-dependent conformational switch of alpha-catenin controls vinculin binding. Nat Commun *5*, 4525.
Yonemura, S., Wada, Y., Watanabe, T., Nagafuchi, A., and Shibata, M. (2010). alpha-Catenin as a tension transducer that induces adherens junction development. Nat Cell Biol *12*, 533-542.
Zaidel-Bar, R., Itzkovitz, S., Ma'ayan, A., Iyengar, R., and Geiger, B. (2007). Functional atlas of the integrin adhesome. Nat Cell Biol *9*, 858-867.
Ziegler, W.H., Liddington, R.C., and Critchley, D.R. (2006). The structure and regulation of vinculin. Trends Cell Biol *16*, 453-460.

Figure legends

Figure 1. Induction of intercellular junction formation positively affects actin reorientation. Control cells were grown in the absence (**A, C**) and presence (**B, D**) of calcium to induce intercellular junction formation and subjected to 4h of cyclic stretch (**C, D**). Arrowheads indicate stretch direction. Scale bar 20 µm. After fixation and staining of actin filaments angular distributions were plotted as cumulative histogram with 0° corresponding to strain direction and 90° perpendicular to it (**E**). (n_A = 157, n_B = 284, n_C = 416 and n_D = 402).

Figure 2. Straining of cell sheets induces loss of FAs. (A) Immunofluorescence micrograph for vinculin, paxillin and actin of $Vinc^{Ctrl}$ cells after 0 h and 4 h of cyclic stretch with different calcium incubation times (0 and 6 h). Arrowheads indicate stretch direction. Scale bar 20 µm. **(B)** Cell area covered with FAs and **(C)** mean FA size for different calcium incubation and stretching times are given ($n_{B\ 0h/0h}$ = 253, $n_{B\ 0h/4h}$ = 238, $n_{B\ 6h/4h}$ = 230, $n_{C\ 0h/0h}$ = 253, $n_{C\ 0h/4h}$ = 234, $n_{C\ 6h/4h}$ = 208).

Figure 3. Actin fibers in cells with cell-cell contacts reorient independent on FAs. (**A-D**) Immunofluorescence micrographs of the actin network of $Vinc^{KO}$ cells grown in the absence (**A+C**) or presence of calcium (**B+D**). For the last 4 h, cells remained either unstretched (**A+B**) or were stretched (**C+D**). Arrowheads indicate stretch direction. Scale bar 20 µm. (**E**) Cumulative histogram showing the angular distributions of actin fiber orientation for the respective experiments (no stretch: $n_{0h\ Ca2+}$ = 368 cells and $n_{6h\ Ca2+}$ = 127; stretch: $n_{0h\ Ca2+}$ = 345 and $n_{6h\ Ca2+}$ = 224). Angular distributions of actin fiber orientation in stretched $Vinc^{Ctrl}$ cells are given for comparison.

Figure 4. Loss of paxillin or talin impairs mechanosensitivity only in the absence of AJs. (**A-D**) Micrographs of paxillin knockdown (Pxn^{KD}, **A, B**) and talin knockdown (Tln^{KD}, **C, D**) cells in low calcium **(A, C)** and high calcium **(B,D)** after 4 h of stretching. Arrowheads indicate stretch direction. Scale bar 20 µm. (**E**) Cumulative histogram showing the angular distributions of actin fiber orientation for the respective experiments ($n_{PxnKD,\ 0\ h\ Ca2+}$ = 1133 cells and $n_{PxnKD,\ 6\ h\ Ca2+}$ = 516, $n_{Tln1/2KD,\ 6h\ Ca2+}$ = 594). WT ($Vinc^{Ctrl}$) distributions from Figure 3 are given for comparison.

Figure 5. Increased actin fiber reorientation is based on AJs and α-catenin as mechanosensor. Immunofluorescence micrographs of the actin network after 4 h of stretch of $ECad^{KO}PCad^{KD}$ cells (**A+B**) and $ECad^{Ctrl}\alpha Cat^{KD}$ cells (**D+E**) grown in the absence (**A+D**) or presence of calcium (**B+E**). Arrowheads indicate stretch direction. Scale bar 20 µm. Cumulative histogram in (**C**) is showing the angular distributions of actin fiber orientation of $ECad^{KO}PCad^{KD}$ single cells (SC) and monolayers (ML) after 4 h of cyclic stretch without (n_{SC} = 277; n_{ML} = 432) and with calcium (n_{SC} = 270; n_{ML} = 421). In (**F**) the same cumulative histogram is given for stretched $ECad^{Ctrl}\alpha Cat^{KD}$ single and monolayer cells without (n_{SC} =

225; n_{ML} = 257) and in the presence of calcium (n_{SC} = 188; n_{ML} = 244). Note: Due to AJ impairment all cells respond to strain just like single cells no matter if Ca^{2+} is present or not.

Figure 6. Mechanosensitivity of AJs depends on α-catenin and its binding partner vinculin. Cumulative histogram showing the angular distributions of actin fiber orientation in WT keratinocytes ($Ecad^{Ctrl}$), cells treated with siRNA against endogenous mouse α-catenin (αCat^{KD}) and same cells with re-incorporated human α-catenin (hαCat) and human α-catenin lacking the vinculin binding domain (ΔVBD). All cells were stretched for 4 h in the absence and presence (6h) of high calcium ($n_{Ctrl\ 0h\ Ca2+}$ = 416; $n_{Ctrl\ 6h\ Ca2+}$ = 305; $n_{\alpha CatKD\ 0h\ Ca2+}$ = 325; $n_{\alpha CatKD\ 6h\ Ca2+}$ = 451; $n_{\Delta vinBD\ 0h\ Ca2+}$ = 372; $n_{\Delta vinBD\ 6h\ Ca2+}$ = 763; $n_{h\alpha Cat\ 0h\ Ca2+}$ = 325; $n_{h\alpha Cat\ 6h\ Ca2+}$ = 662). **(B)** Angular distributions of actin fiber orientation in $Vinc^{KO}\alpha Cat^{KD}$ cells with impaired FA- and AJ-dependent mechanosensitivity were plotted as cumulative histogram. Cells were stretched for 4 h in the absence or presence of calcium for 6 h (n=250). Distributions of $Vinc^{KO}$ alone are given for comparison. Note the strongly reduced reorientation behavior of actin filaments in $Vinc^{KO}\alpha Cat^{KD}$ cells also for monolayer grown in high calcium.

Figure 7. FA/AJ interplay model in mechanosensation. Keratinocytes in monolayers and low calcium conditions (top, left) are adhered via FAs to the substrate. Cell-cell contacts are barely formed. Upon stretching in low calcium medium (top, right) FAs function as mechanosensitive elements, causing stress fiber reorientation without changing FAs as main adhesion structure. Cells remain largely separated without forming zipper-like cell-cell contacts. In contrast, when cells are incubated in high calcium, epithelial sheet formation is induced (bottom, left) leading to zipper-like formation of AJs in apical cell regions and thereby reduced cell gaps, partial disassembly of FAs, incorporation of vinculin into AJs and actin filament relocalization to the cell periphery with contacts to AJs. Upon stretching of epithelial sheets (bottom, right), further FA disassembly takes place which is accompanied with translocation of mechanosensitive function from FAs to AJs. AJ-dependent strain recognition largely depends on α-catenin and attached vinculin and leads to highly parallelized actin filaments spanning the cells completely with angles being distributed sharply around perpendicular direction relative to strain and therefore higher angles than known for FA-dependent reorientations. For better visualization an animation is given as Supplementary movie 1.

Supplementary Information:

Supplementary Figure 1: Estimation of confidence intervals. Actin reorientation angles for all experimental conditions and cell types presented in Figures 1, 3, 4, 5, 6 and Supplementary Figures 3 and 5 were statistically analyzed using bootstrapping. Bootstrap sample size was set to 5000 based on the indicated high numbers of analyzed cells. Estimated upper and lower 95% confidence intervals as well as actual cumulated frequencies are given for classes of 10° each.

Supplementary Figure 2. Calcium influences FA composition and actin fiber organization. Immunofluorescence micrographs showing the apical and basal layer of $Vinc^{Crtl}$ cells after growth without (**A**) and with (**B**) calcium. Scale bar 20 µm. (**C**) Cell area covered with FAs for different calcium incubation times (n_{0h} = 159; n_{2h} = 83; n_{6h} = 167; n_{24h} = 119). (**D**) Co-localization of vinculin and paxillin in FAs of the basal layer of $Vinc^{Ctrl}$ cells for different calcium incubation times (n_{0h} = 67; n_{2h} = 57; n_{6h} = 41; n_{24h} = 13). (**E**) Histograms showing the distribution of the actin arrangement parameter without (left; n = 170) and with (right; n = 83) calcium. Positive values (light grey) indicate high actin concentration in the cellular periphery compared to its center and vice versa (negative values = dark grey.

Supplementary Figure 3. Formation of cell-cell contacts accelerates actin fiber reorientation. Immunofluorescence micrographs of the actin network of single cells with $Vinc^{Ctrl}$ (**A+B**) or $Vinc^{KO}$ (**C+D**) genetic background. All cells were stretched for 4 hours in the absence (**A+D**) or presence (**B+E**) of Ca^{2+}. Arrowheads indicate stretch direction. Scale bar 20 µm. Cumulative histogram showing the angular distributions of actin fiber orientation for the respective experiments in monolayers (ML) and single cells (SC) of $Vinc^{Ctrl}$ cells (**C**) after cyclic stretch (4 h) without (n_{SC} = 214; n_{ML} = 201) and with calcium (n_{SC} = 243; n_{ML} = 178). Same cumulative histograms are also given for $Vinc^{KO}$ cells (**F**) after cyclic stretch (4 h) without (n_{SC} = 229; n_{ML} = 225) and with calcium (n_{SC} = 162; n_{ML} = 185).

Supplementary Figure 4. Verification of knockdown efficiencies by western blotting. Crude protein extracts of indicated strains were tested for (**A**) remaining P-Cadherin levels, (**B**) knockdown efficiencies of paxillin (Pxn^{KD}), (**C**) α-catenin (α-cat), and (**D**) talin1/2 isoforms ($Tln_{1/2}^{KD}$). Furthermore in (**C**) α-$catenin^{KD}$ cells were analyzed for efficient expression of reincorporated human α-catenin (hαCat) and human α-catenin lacking the vinculin binding domain (ΔvinBD). Re-expressed proteins were additionally detected by their c-Myc tag. Tubulin was used as constitutively expressed marker protein for all western analyses. Normalized remaining protein levels are indicated.

Supplementary Figure 5. Knock-out of E-cadherin alone is not sufficient to inhibit AJ-dependent reorientation. Immunofluorescence micrographs of the actin network of $ECad^{Ctrl}$ (**A-D**) or $ECad^{KO}$ (**F-I**) cells grown as single cell (**A+B, F+G**) or as monolayer (**C+D, H+I**). All cells were stretched for 4 hours in the absence (**A+C, F+H**) or presence (**B+D, G+I**) of Ca^{2+}. Arrowheads indicate stretch direction. Scale bar 20 µm. (**E**) Cumulative histogram showing the angular distributions of actin fiber orientation of $ECad^{Ctrl}$ single cells (SC) and monolayers (ML) after 4 h of cyclic stretch without (n_{SC} = 400; n_{ML} = 528) and with calcium (n_{SC} = 409; n_{ML} = 501). **(J)** Cumulative histogram showing the angular distributions of actin fiber orientation in $ECad^{KO}$ cells after 4 h of cyclic stretch without (n_{SC} = 201; n_{ML} = 212) and with calcium (n_{SC} = 217; n_{ML} =154).

Supplementary Figure 6. Cell sheet formation increases cadherin expression. (A) Immunofluorescence micrographs of $ECad^{Ctrl}$ and $ECad^{KO}$ cells after incubation for 24 h in high calcium using an antibody against E-cadherin with some cross-reactivity to P-cadherin. **(B)** Western blot analysis of respective crude protein extracts for cadherin concentration. Tubulin is used as standard. Note the increase in cadherin concentration after cell sheet formation even in $ECad^{KO}$ cells. Scale bar 20 µm.

Supplementary Movie 1. FA/AJ interplay model in mechanosensation. The movie shows cells under low calcium conditions without applied stretch. For detailed description see Figure 7.

Supplementary Movie 2. FA/AJ interplay model in mechanosensation. The movie shows stretched cells under low calcium conditions. For detailed description see Figure 7.

Supplementary Movie 3. FA/AJ interplay model in mechanosensation. The movie shows cells under high calcium conditions without applied stretch. For detailed description see Figure 7.

Supplementary Movie 4. FA/AJ interplay model in mechanosensation. The movie shows stretched cells under high calcium conditions. For detailed description see Figure 7.

Figures

Figure 1

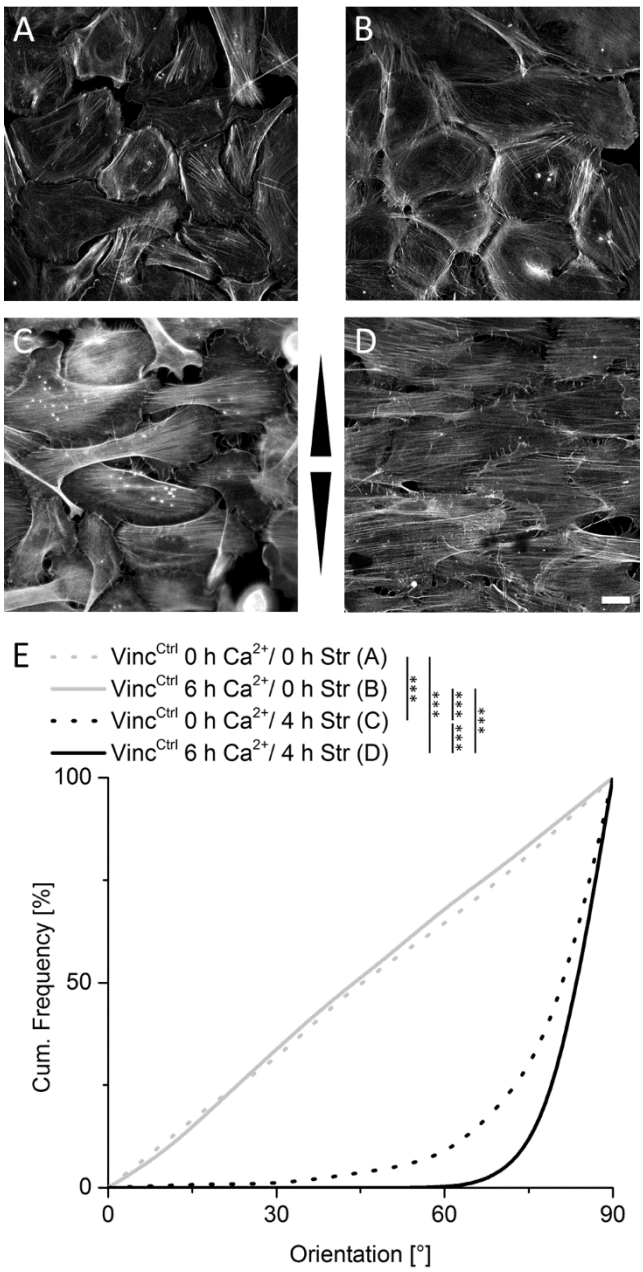

Figure 2

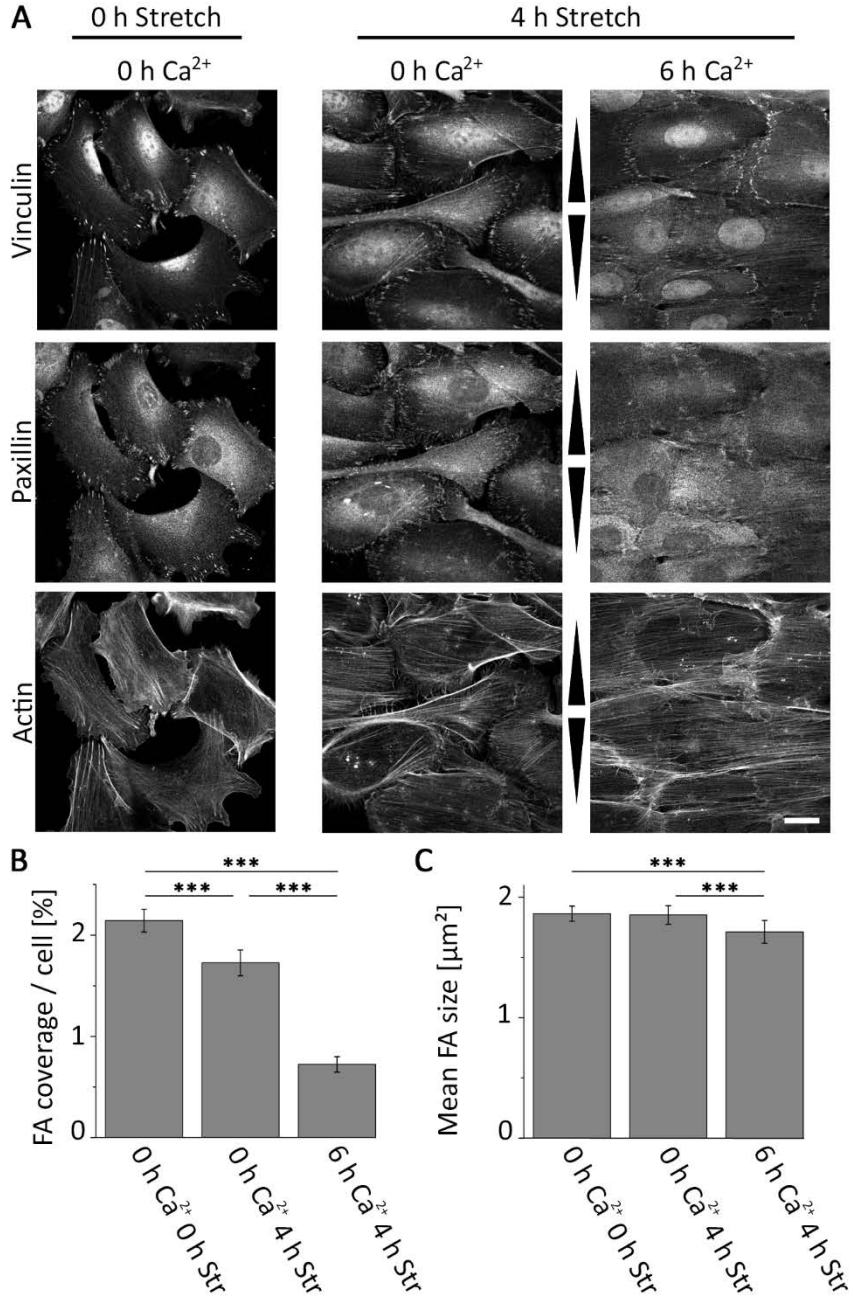
A
0 h Stretch
4 h Stretch
0 h Ca2+
0 h Ca2+
6 h Ca2+
Vinculin
Paxillin
Actin
B
FA coverage / cell [%]
***
***
***
0
1
2
0 h Ca2+ 0 h Str
0 h Ca2+ 4 h Str
6 h Ca2+ 4 h Str
C
Mean FA size [µm²]
***
***
0
1
2
0 h Ca2+ 0 h Str
0 h Ca2+ 4 h Str
6 h Ca2+ 4 h Str

Figure 3

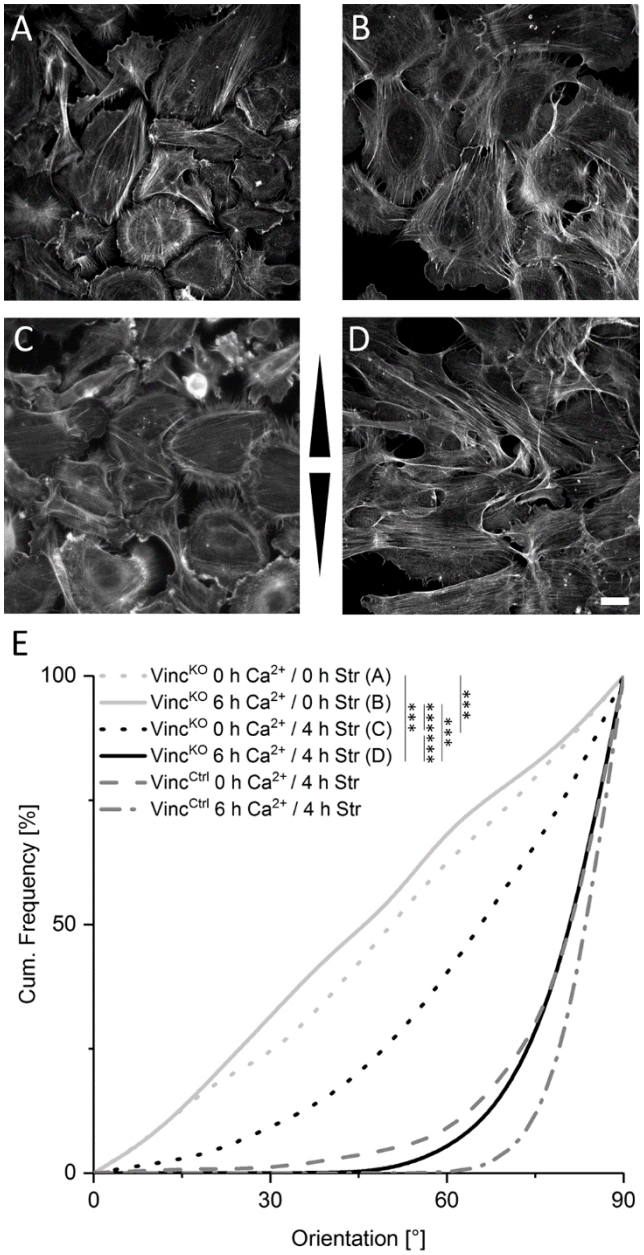
A
B
C
D
E
100
50
0
Cum. Frequency [%]
0
30
60
90
Orientation [°]
Vinc^KO 0 h Ca2+ / 0 h Str (A)
Vinc^KO 6 h Ca2+ / 0 h Str (B)
Vinc^KO 0 h Ca2+ / 4 h Str (C)
Vinc^KO 6 h Ca2+ / 4 h Str (D)
Vinc^Ctrl 0 h Ca2+ / 4 h Str
Vinc^Ctrl 6 h Ca2+ / 4 h Str
***
***
***
***

Figure 4

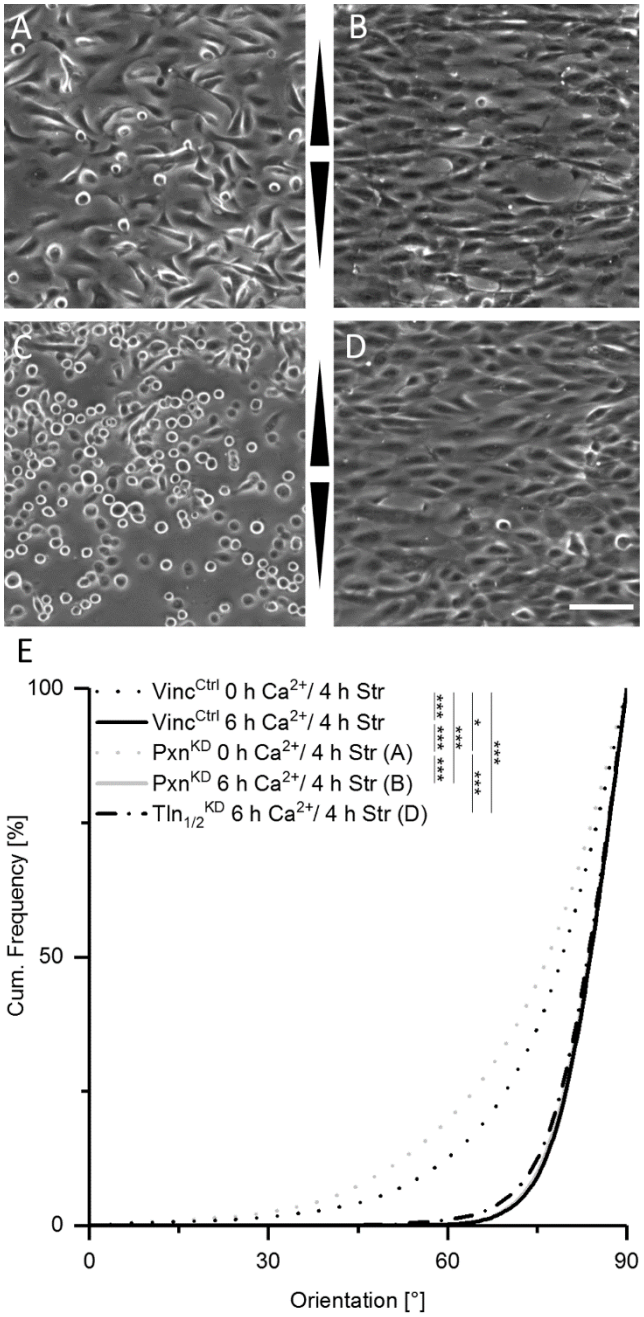
A
B
C
D
E
100
50
0
Cum. Frequency [%]
0
30
60
90
Orientation [°]
Vinc^Ctrl 0 h Ca2+/ 4 h Str
Vinc^Ctrl 6 h Ca2+/ 4 h Str
Pxn^KD 0 h Ca2+/ 4 h Str (A)
Pxn^KD 6 h Ca2+/ 4 h Str (B)
Tln1/2^KD 6 h Ca2+/ 4 h Str (D)
***
***
***
***
*
***

Figure 5

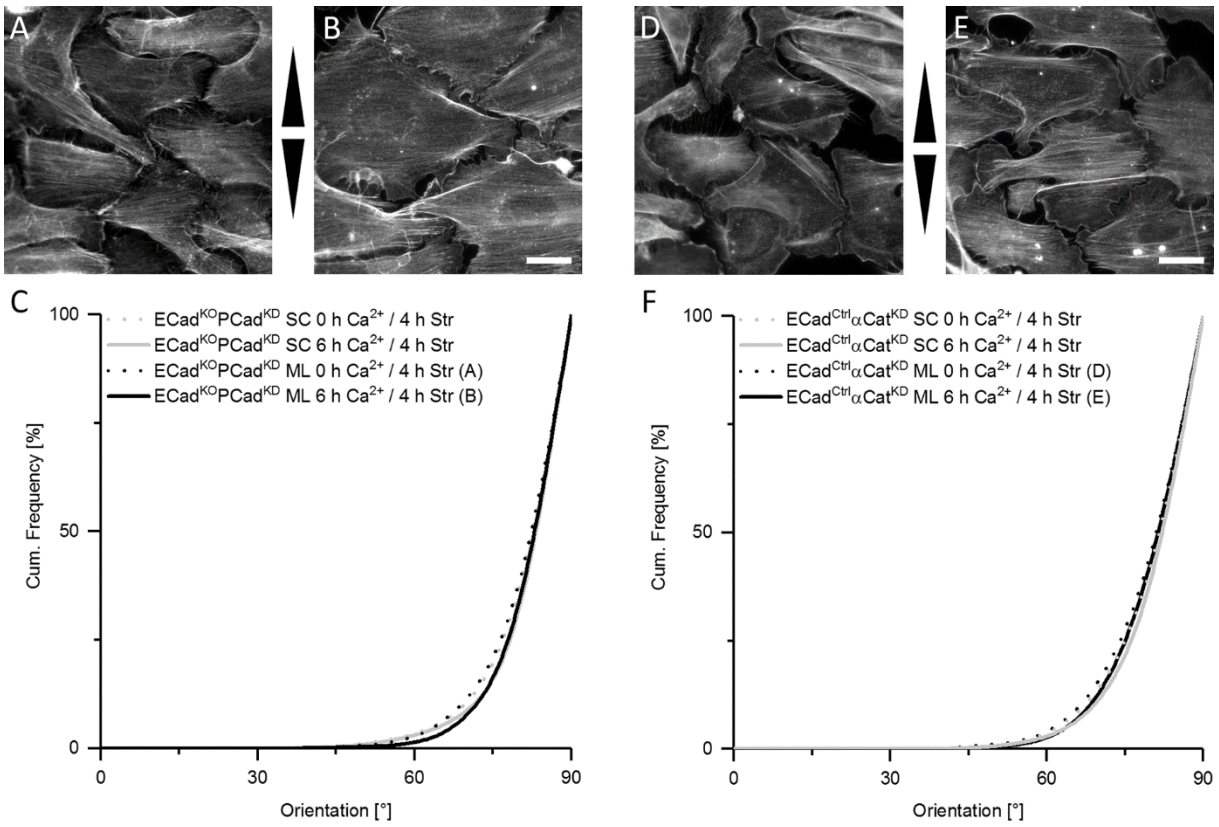
A
B
D
E
C
F
ECad^KO PCad^KD SC 0 h Ca2+ / 4 h Str
ECad^KO PCad^KD SC 6 h Ca2+ / 4 h Str
ECad^KO PCad^KD ML 0 h Ca2+ / 4 h Str (A)
ECad^KO PCad^KD ML 6 h Ca2+ / 4 h Str (B)
ECad^Ctrl αCat^KD SC 0 h Ca2+ / 4 h Str
ECad^Ctrl αCat^KD SC 6 h Ca2+ / 4 h Str
ECad^Ctrl αCat^KD ML 0 h Ca2+ / 4 h Str (D)
ECad^Ctrl αCat^KD ML 6 h Ca2+ / 4 h Str (E)
Cum. Frequency [%]
Orientation [°]
0
30
60
90
50
100

Figure 6

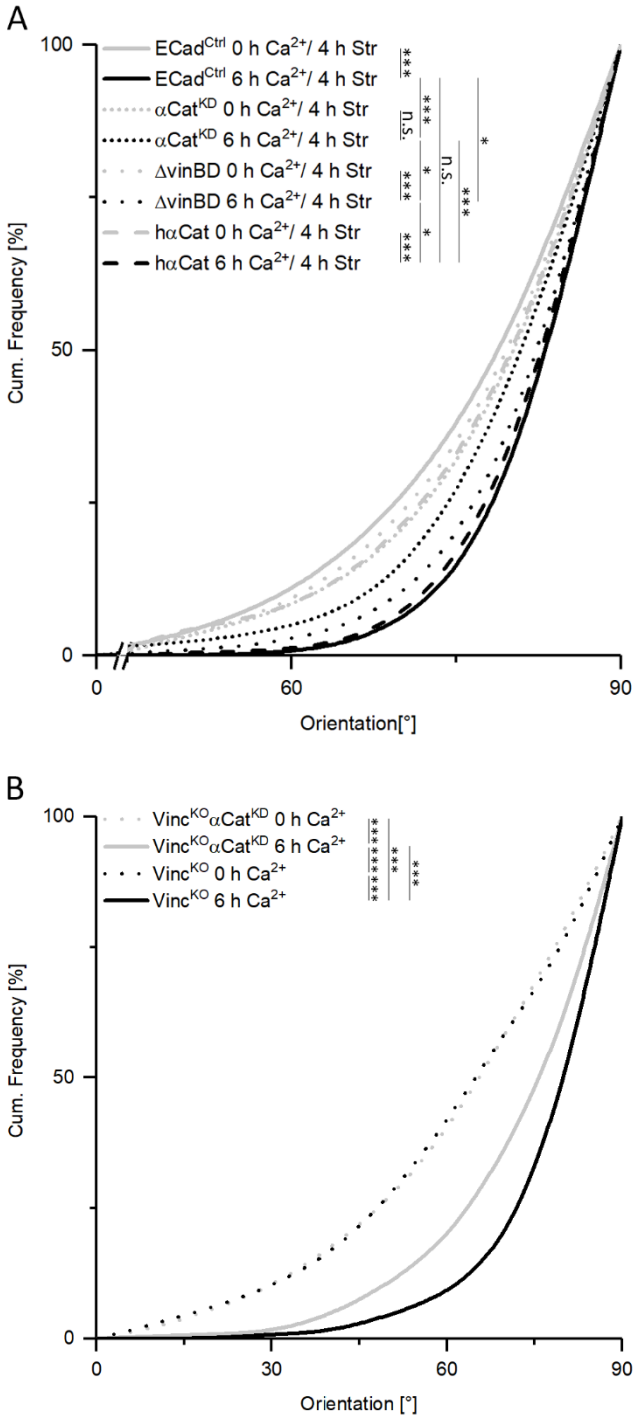
A
100
50
0
Cum. Frequency [%]
0
60
90
Orientation[°]
ECad^Ctrl 0 h Ca2+/ 4 h Str
ECad^Ctrl 6 h Ca2+/ 4 h Str
αCat^KD 0 h Ca2+/ 4 h Str
αCat^KD 6 h Ca2+/ 4 h Str
ΔvinBD 0 h Ca2+/ 4 h Str
ΔvinBD 6 h Ca2+/ 4 h Str
hαCat 0 h Ca2+/ 4 h Str
hαCat 6 h Ca2+/ 4 h Str
***
n.s.
***
*
n.s.
***
*
***
*
B
100
50
0
Cum. Frequency [%]
0
30
60
90
Orientation [°]
Vinc^KOαCat^KD 0 h Ca2+
Vinc^KOαCat^KD 6 h Ca2+
Vinc^KO 0 h Ca2+
Vinc^KO 6 h Ca2+
***
***
***
***

Figure 7

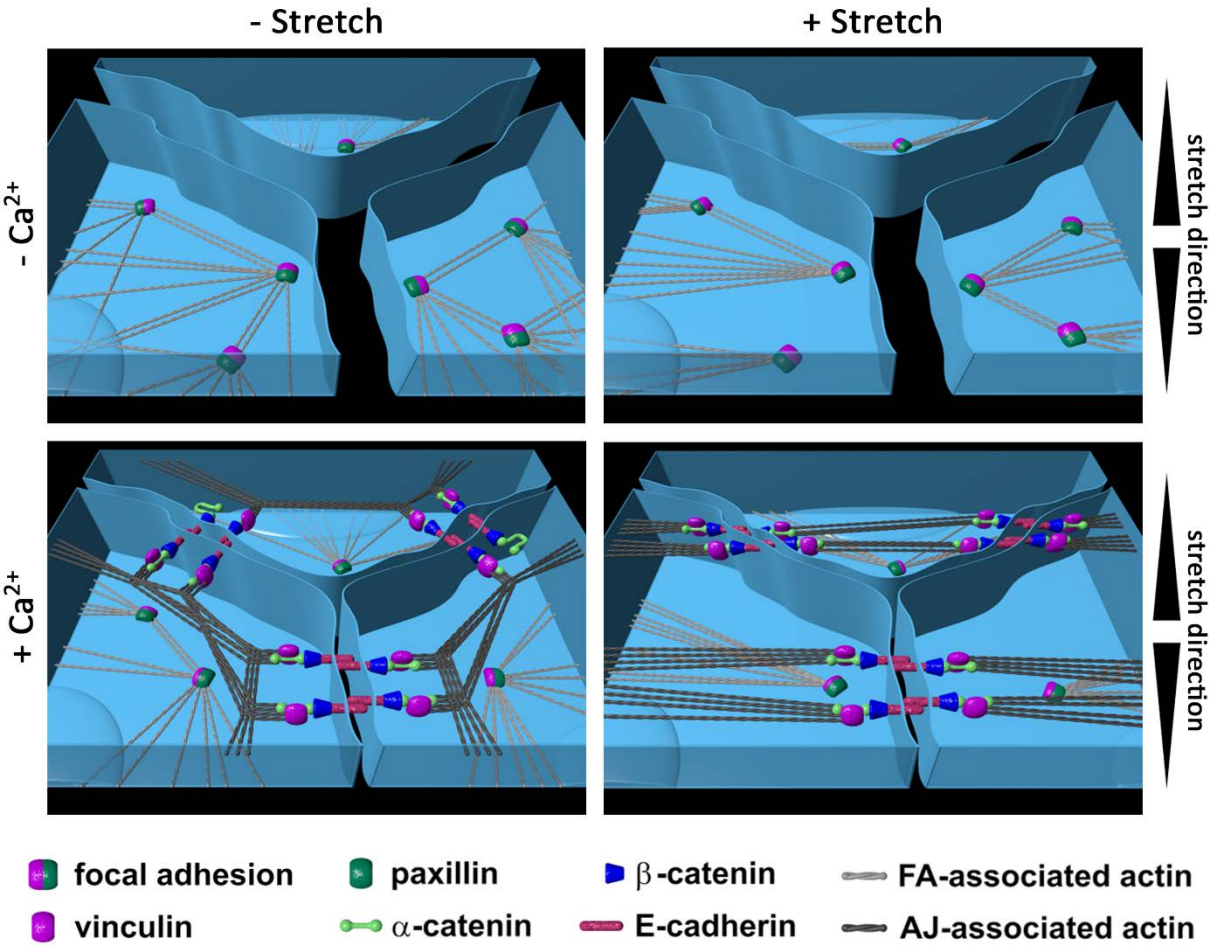
- Stretch
+ Stretch
- Ca2+
+ Ca2+
stretch direction
stretch direction
focal adhesion
paxillin
β-catenin
FA-associated actin
vinculin
α-catenin
E-cadherin
AJ-associated actin

Supplementary Figure 1

Table S1. Estimation of the 95% confidence intervals (CI95) for cumulative histograms in Fig.1

Vinc^{Ctrl} 0h Ca^{2+} / 0h Stretch (n=157)

Class	Lower CI95	Cum. Frequency	Upper CI95
10	0.064	0.11	0.17
20	0.15	0.22	0.39
30	0.24	0.31	0.39
40	0.36	0.45	0.53
50	0.46	0.55	0.63
60	0.56	0.64	0.72
70	0.68	0.75	0.82
80	0.81	0.87	0.92
90	1	1	1

Vinc^{Ctrl} 0h Ca^{2+} / 4h Stretch (n=416)

Class	Lower CI95	Cum. Frequency	Upper CI95
10	0	0.0053	0.016
20	0	0.0088	0.022
30	0	0.0088	0.022
40	0.01	0.026	0.046
50	0.026	0.046	0.071
60	0.049	0.076	0.11
70	0.15	0.19	0.24
80	0.34	0.39	0.44
90	1	1	1

Vinc^{Ctrl} 6h Ca^{2+} / 0h Stretch (n=284)

Class	Lower CI95	Cum. Frequency	Upper CI95
10	0.055	0.084	0.12
20	0.16	0.21	0.27
30	0.28	0.34	0.04
40	0.40	0.46	0.53
50	0.50	0.56	0.63
60	0.62	0.68	0.74
70	0.73	0.78	0.84
80	0.85	0.89	0.93
90	1	1	1

Vinc^{Ctrl} 6h Ca^{2+} / 0h Stretch (n=402)

Class	Lower CI95	Cum. Frequency	Upper CI95
10	0	0	0
20	0	0	0
30	0	0	0
40	0	0	0
50	0	0	0
60	0	0	0
70	0.0071	0.02	0.032
80	0.15	0.19	0.23
90	1	1	1

The 95% confidence intervals for the cumulative histograms were estimated by using the method for bias-corrected and accelerated (BCa) bootstrap intervals. The number of bootstrap samples for each histogram was 5000.

Table S2. Estimation of the 95% confidence intervals (CI95) for cumulative histograms in Fig. 3

Vinc^{KO} 0h Ca^{2+} / 0h Stretch (n=368)

Class	Lower CI95	Cum. Frequency	Upper CI95
10	0.049	0.07	0.11
20	0.14	0.18	0.23
30	0.19	0.23	0.28
40	0.30	0.35	0.40
50	0.44	0.49	0.55
60	0.58	0.63	0.69
70	0.68	0.73	0.78
80	0.82	0.86	0.9
90	1	1	1

Vinc^{KO} 0h Ca^{2+} / 4h Stretch (n=345)

Class	Lower CI95	Cum. Frequency	Upper CI95
10	0.0058	0.018	0.036
20	0.020	0.039	0.063
30	0.06	0.092	0.13
40	0.11	0.15	0.19
50	0.20	0.25	0.30
60	0.34	0.40	0.45
70	0.52	0.58	0.63
80	0.69	0.74	0.79
90	1	1	1

Vinc^{KO} 6h Ca^{2+} / 0h Stretch (n=127)

Class	Lower CI95	Cum. Frequency	Upper CI95
10	0.031	0.071	0.13
20	0.12	0.19	0.27
30	0.23	0.31	0.41
40	0.35	0.44	0.53
50	0.44	0.54	0.62
60	0.60	0.69	0.77
70	0.69	0.78	0.85
80	0.79	0.87	0.92
90	1	1	1

Vinc^{KO} 6h Ca^{2+} / 4h Stretch (n=224)

Class	Lower CI95	Cum. Frequency	Upper CI95
10	0	0	0
20	0	0	0
30	0	0	0
40	0	0	0
50	0	0.005	0.019
60	0.022	0.045	0.077
70	0.10	0.14	0.20
80	0.34	0.41	0.48
90	1	1	1

The 95% confidence intervals for the cumulative histograms were estimated by using the method for bias-corrected and accelerated (BCa) bootstrap intervals. The number of bootstrap samples for each histogram was 5000.

Table S3. Estimation of the 95% confidence intervals (CI95) for cumulative histograms in Fig. 4

Vinc^{Ctrl} 0h Ca^{2+} (n=135)

Class	Lower CI95	Cum. Frequency	Upper CI95
10	0	0.0074	0.030
20	0	0.0074	0.030
30	0	0.015	0.038
40	0.0074	0.030	0.067
50	0.022	0.052	0.097
60	0.074	0.12	0.18
70	0.16	0.23	0.31
80	0.4	0.49	0.58
90	1	1	1

Vinc^{Ctrl} 6h Ca^{2+} (n=412)

Class	Lower CI95	Cum. Frequency	Upper CI95
10	0	0	0
20	0	0	0
30	0	0	0
40	0	0	0
50	0	0	0
60	0	0	0
70	0.0024	0.010	0.022
80	0.10	0.14	0.18
90	1	1	1

Pxn^{KD} 0h Ca^{2+} (n=1133)

Class	Lower CI95	Cum. Frequency	Upper CI95
10	0.0026	0.0071	0.013
20	0.0070	0.012	0.021
30	0.015	0.024	0.034
40	0.035	0.046	0.060
50	0.083	0.10	0.12
60	0.16	0.19	0.22
70	0.30	0.33	0.36
80	0.54	0.57	0.6
90	1	1	1

Pxn^{KD} 6h Ca^{2+} (n=516)

Class	Lower CI95	Cum. Frequency	Upper CI95
10	0	0	0
20	0	0	0
30	0	0	0
40	0	0	0
50	0	0	0
60	0	0	0
70	0.0058	0.014	0.026
80	0.12	0.16	0.19
90	1	1	1

Tln^{KD} 6h Ca^{2+} (n=594)

Class	Lower CI95	Cum. Frequency	Upper CI95
10	0	0	0
20	0	0	0
30	0	0	0
40	0	0	0
50	0	0	0
60	0.0016	0.0084	0.017
70	0.013	0.024	0.038
80	0.14	0.17	0.21
90	1	1	1

The 95% confidence intervals for the cumulative histograms were estimated by using the method for bias-corrected and accelerated (BCa) bootstrap intervals. The number of bootstrap samples for each histogram was 5000.

Table S4. Estimation of the 95% confidence intervals (CI95) for cumulative histograms in Fig. 5

ECad^{KO}PCad^{KD} 0h Ca^{2+} SC (n=277)

Class	Lower CI95	Cum. Frequency	Upper CI95
10	0	0	0
20	0	0	0
30	0	0	0
40	0	0	0
50	0	0.0072	0.019
60	0.0036	0.018	0.037
70	0.036	0.062	0.093
80	0.22	0.27	0.33
90	1	1	1

ECad^{KO}PCad^{KD} 6h Ca^{2+} SC (n=270)

Class	Lower CI95	Cum. Frequency	Upper CI95
10	0	0	0
20	0	0	0
30	0	0	0
40	0	0	0
50	0	0.0035	0.015
60	0.0036	0.018	0.036
70	0.036	0.062	0.096
80	0.18	0.23	0.29
90	1	1	1

ECad^{KO}PCad^{KD} 0h Ca^{2+} ML (n=432)

Class	Lower CI95	Cum. Frequency	Upper CI95
10	0	0	0
20	0	0	0
30	0	0	0
40	0	0	0
50	0	0.0040	0.017
60	0.0046	0.014	0.028
70	0.055	0.081	0.11
80	0.22	0.27	0.32
90	1	1	1

ECad^{KO}PCad^{KD} 6h Ca^{2+} ML (n=421)

Class	Lower CI95	Cum. Frequency	Upper CI95
10	0	0	0
20	0	0	0
30	0	0	0
40	0	0	0
50	0	0.0023	0.0091
60	0	0.0046	0.012
70	0.028	0.047	0.070
80	0.21	0.26	0.31
90	1	1	1

αCat^{KD} 0h Ca^{2+} SC (n=225)

Class	Lower CI95	Cum. Frequency	Upper CI95
10	0	0	0
20	0	0	0
30	0	0	0
40	0	0.0027	0.011
50	0	0.0027	0.011
60	0.015	0.041	0.088
70	0.092	0.14	0.21
80	0.30	0.39	0.47
90	1	1	1

αCat^{KD} 6h Ca^{2+} SC (n=188)

Class	Lower CI95	Cum. Frequency	Upper CI95
10	0	0	0
20	0	0	0
30	0	0	0
40	0	0	0
50	0	0.0068	0.018
60	0.010	0.034	0.066
70	0.072	0.12	0.17
80	0.29	0.37	0.44
90	1	1	1

αCat^{KD} 0h Ca^{2+} ML (n=257)			
Class	Lower CI95	Cum. Frequency	Upper CI95
10	0	0	0
20	0	0	0
30	0	0	0
40	0	0	0
50	0	0.0086	0.27
60	0.0058	0.023	0.048
70	0.10	0.14	0.19
80	0.35	0.41	0.48
90	1	1	1

αCat^{KD} 6h Ca^{2+} ML (n=244)			
Class	Lower CI95	Cum. Frequency	Upper CI95
10	0	0	0
20	0	0	0
30	0	0	0
40	0	0	0
50	0	0.0051	0.021
60	0.0051	0.021	0.041
70	0.070	0.11	0.15
80	0.34	0.41	0.48
90	1	1	1

The 95% confidence intervals for the cumulative histograms were estimated by using the method for bias-corrected and accelerated (BCa) bootstrap intervals. The number of bootstrap samples for each histogram was 5000.

Table S5. Estimation of the 95% confidence intervals (CI95) for cumulative histograms in Fig. 6

ECad^{Ctrl} 0h Ca^{2+} (n=416)

Class	Lower CI95	Cum. Frequency	Upper CI95
10	0	0.0026	0.011
20	0	0.0026	0.011
30	0.0026	0.012	0.026
40	0.0048	0.015	0.030
50	0.018	0.033	0.053
60	0.070	0.098	0.13
70	0.20	0.243	0.29
80	0.45	0.506	0.56
90	1	1	1

ECad^{Ctrl} 6h Ca^{2+} (n=305)

Class	Lower CI95	Cum. Frequency	Upper CI95
10	0	0	0
20	0	0	0
30	0	0	0
40	0	0	0
50	0	0	0
60	0	0.0027	0.011
70	0.019	0.037	0.060
80	0.18	0.23	0.28
90	1	1	1

αCat^{KD} 0h Ca^{2+} (n=325)

Class	Lower CI95	Cum. Frequency	Upper CI95
10	0	0	0
20	0	0	0
30	0	0.0048	0.013
40	0	0.0048	0.013
50	0.010	0.030	0.054
60	0.045	0.074	0.11
70	0.13	0.18	0.23
80	0.38	0.44	0.5
90	1	1	1

αCat^{KD} 6h Ca^{2+} (n=451)

Class	Lower CI95	Cum. Frequency	Upper CI95
10	0	0.0048	0.015
20	0.0024	0.011	0.023
30	0.0024	0.011	0.023
40	0.0061	0.016	0.030
50	0.0089	0.020	0.035
60	0.025	0.043	0.074
70	0.086	0.11	0.15
80	0.36	0.41	0.46
90	1	1	1

ΔvinBD 0h Ca^{2+} (n=372)

Class	Lower CI95	Cum. Frequency	Upper CI95
10	0	0	0
20	0	0.0033	0.014
30	0	0.0056	0.016
40	0.0022	0.011	0.025
50	0.015	0.032	0.055
60	0.052	0.079	0.11
70	0.17	0.22	0.26
80	0.41	0.47	0.52
90	1	1	1

ΔvinBD 6h Ca^{2+} (n=763)

Class	Lower CI95	Cum. Frequency	Upper CI95
10	0	0	0
20	0	0	0
30	0	0	0
40	0	0.0036	0.0086
50	0.0027	0.0080	0.16
60	0.011	0.021	0.033
70	0.058	0.076	0.096
80	0.27	0.30	0.34
90	1	1	1

hαCat^{KD} 0h Ca^{2+} (n=325)

Class	Lower CI95	Cum. Frequency	Upper CI95
10	0	0	0
20	0	0	0
30	0	0	0
40	0	0.0090	0.022
50	0.024	0.045	0.70
60	0.044	0.069	0.10
70	0.15	0.19	0.24
80	0.39	0.45	0.51
90	1	1	1

hαCat^{KD} 6h Ca^{2+} (n=662)

Class	Lower CI95	Cum. Frequency	Upper CI95
10	0	0	0
20	0	0	0
30	0	0	0
40	0	0	0
50	0	0.0049	0.014
60	0.0019	0.0074	0.017
70	0.026	0.041	0.059
80	0.23	0.27	0.31
90	1	1	1

Vinc^{KO} 0h Ca^{2+} (n=250)

Class	Lower CI95	Cum. Frequency	Upper CI95
10	0.012	0.028	0.052
20	0.032	0.060	0.092
30	0.068	0.10	0.14
40	0.12	0.16	0.22
50	0.21	0.27	0.33
60	0.35	0.42	0.48
70	0.52	0.59	0.65
80	0.69	0.75	0.81
90	1	1	1

Vinc^{KO} 6h Ca^{2+} (n=250)

Class	Lower CI95	Cum. Frequency	Upper CI95
10	0	0	0
20	0	0	0
30	0	0.0080	0.024
40	0	0.012	0.028
50	0.02	0.044	0.072
60	0.052	0.084	0.12
70	0.13	0.18	0.23
80	0.4	0.46	0.53
90	1	1	1

Vinc^{KO}αCat^{KD} 0h Ca^{2+} (n=250)

Class	Lower CI95	Cum. Frequency	Upper CI95
10	0.008	0.020	0.04
20	0.028	0.056	0.084
30	0.064	0.10	0.14
40	0.12	0.17	0.22
50	0.20	0.26	0.32
60	0.33	0.40	0.46
70	0.52	0.58	0.65
80	0.72	0.78	0.83
90	1	1	1

Vinc^{KO}αCat^{KD} 6h Ca^{2+} (n=250)

Class	Lower CI95	Cum. Frequency	Upper CI95
10	0	0.0040	0.016
20	0	0.0080	0.02
30	0	0.012	0.028
40	0.024	0.044	0.072
50	0.068	0.10	0.14
60	0.14	0.19	0.24
70	0.29	0.36	0.42
80	0.53	0.60	0.66
90	1	1	1

The 95% confidence intervals for the cumulative histograms were estimated by using the method for bias-corrected and accelerated (BCa) bootstrap intervals. The number of bootstrap samples for each histogram was 5000.

Table S6. Estimation of the 95% confidence intervals (CI95) for cumulative histograms in Supplementary Fig. 3

Vinc^{Ctrl} 0h Ca^{2+} SC (n=214)

Class	Lower CI95	Cum. Frequency	Upper CI95
10	0	0.007	0.029
20	0.0034	0.018	0.043
30	0.0069	0.025	0.050
40	0.017	0.040	0.071
50	0.042	0.076	0.12
60	0.079	0.12	0.17
70	0.15	0.20	0.26
80	0.33	0.41	0.48
90	1	1	1

Vinc^{Ctrl} 6h Ca^{2+} SC (n=243)

Class	Lower CI95	Cum. Frequency	Upper CI95
10	0	0	0.015
20	0	0.012	0.030
30	0	0.012	0.030
40	0.0079	0.024	0.047
50	0.020	0.045	0.075
60	0.043	0.075	0.12
70	0.10	0.15	0.20
80	0.28	0.34	0.41
90	1	1	1

Vinc^{Ctrl} 0h Ca^{2+} ML (n=201)

Class	Lower CI95	Cum. Frequency	Upper CI95
10	0	0	0
20	0	0	0
30	0	0	0
40	0	0	0
50	0	0.018	0.045
60	0.029	0.063	0.11
70	0.081	0.13	0.19
80	0.29	0.36	0.44
90	1	1	1

Vinc^{Ctrl} 6h Ca^{2+} ML (n=178)

Class	Lower CI95	Cum. Frequency	Upper CI95
10	0	0	0
20	0	0	0
30	0	0	0
40	0	0	0.019
50	0	0.0090	0.028
60	0	0.0090	0.028
70	0	0.016	0.041
80	0.095	0.15	0.21
90	1	1	1

Vinc^{KO} 0h Ca^{2+} SC (n=229)

Class	Lower CI95	Cum. Frequency	Upper CI95
10	0.011	0.029	0.055
20	0.021	0.046	0.077
30	0.072	0.11	0.16
40	0.14	0.20	0.25
50	0.23	0.29	0.36
60	0.33	0.40	0.47
70	0.51	0.58	0.65
80	0.72	0.78	0.83
90	1	1	1

Vinc^{KO} 6h Ca^{2+} SC (n=162)

Class	Lower CI95	Cum. Frequency	Upper CI95
10	0.016	0.042	0.077
20	0.05	0.090	0.14
30	0.073	0.12	0.18
40	0.098	0.15	0.21
50	0.14	0.21	0.27
60	0.27	0.34	0.42
70	0.41	0.49	0.57
80	0.59	0.67	0.75
90	1	1	1

Vinc^{KO} 0h Ca^{2+} ML (n=225)

Class	Lower CI95	Cum. Frequency	Upper CI95
10	0	0.014	0.037
20	0.014	0.041	0.079
30	0.041	0.081	0.13
40	0.069	0.12	0.17
50	0.14	0.19	0.26
60	0.25	0.32	0.40
70	0.39	0.47	0.54
80	0.63	0.70	0.77
90	1	1	1

Vinc^{KO} 6h Ca^{2+} ML (n=185)

Class	Lower CI95	Cum. Frequency	Upper CI95
10	0	0.0090	0.028
20	0	0.0090	0.028
30	0	0.014	0.032
40	0.0045	0.023	0.046
50	0.0090	0.027	0.050
60	0.031	0.06	0.091
70	0.15	0.20	0.27
80	0.40	0.48	0.55
90	1	1	1

The 95% confidence intervals for the cumulative histograms were estimated by using the method for bias-corrected and accelerated (BCa) bootstrap intervals. The number of bootstrap samples for each histogram was 5000.

Table S7. Estimation of the 95% confidence intervals (CI95) for cumulative histograms in Supplementary Fig. 5

ECad^{Ctrl} 0h Ca^{2+} SC (n=400)

Class	Lower CI95	Cum. Frequency	Upper CI95
10	0	0.0075	0.018
20	0.0025	0.013	0.025
30	0.01	0.023	0.04
40	0.0125	0.028	0.045
50	0.025	0.043	0.063
60	0.057	0.085	0.12
70	0.10	0.14	0.18
80	0.27	0.32	0.37
90	1	1	1

ECad^{Ctrl} 6h Ca^{2+} SC (n=409)

Class	Lower CI95	Cum. Frequency	Upper CI95
10	0	0	0
20	0	0.0024	0.0098
30	0	0.0024	0.0098
40	0.0024	0.0098	0.023
50	0.0073	0.020	0.035
60	0.031	0.051	0.074
70	0.088	0.12	0.16
80	0.23	0.28	0.33
90	1	1	1

ECad^{Ctrl} 0h Ca^{2+} ML (n=528)

Class	Lower CI95	Cum. Frequency	Upper CI95
10	0	0.0038	0.012
20	0	0.0038	0.012
30	0	0.0057	0.014
40	0	0.0057	0.014
50	0.0094	0.019	0.033
60	0.0028	0.045	0.065
70	0.010	0.13	0.17
80	0.32	0.36	0.41
90	1	1	1

ECad^{Ctrl} 6h Ca^{2+} ML (n=501)

Class	Lower CI95	Cum. Frequency	Upper CI95
10	0	0	0
20	0	0	0
30	0	0	0
40	0	0	0
50	0	0	0
60	0	0	0
70	0.0079	0.018	0.032
80	0.13	0.17	0.21
90	1	1	1

ECad^{KO} 0h Ca^{2+} SC (n=201)

Class	Lower CI95	Cum. Frequency	Upper CI95
10	0	0	0
20	0	0.0068	0.028
30	0	0.017	0.042
40	0.0035	0.021	0.045
50	0.026	0.054	0.092
60	0.053	0.091	0.14
70	0.11	0.15	0.21
80	0.29	0.35	0.43
90	1	1	1

ECad^{KO} 6h Ca^{2+} SC (n=217)

Class	Lower CI95	Cum. Frequency	Upper CI95
10	0	0	0
20	0	0	0
30	0	0	0
40	0	0.0032	0.013
50	0	0.015	0.040
60	0.024	0.053	0.088
70	0.091	0.14	0.19
80	0.28	0.35	0.43
90	1	1	1

ECad^{KO} 0h Ca^{2+} ML (n=212)				ECad^{KO} 6h Ca^{2+} ML (n=154)			
Class	Lower CI95	Cum. Frequency	Upper CI95	Class	Lower CI95	Cum. Frequency	Upper CI95
10	0	0	0	10	0	0	0
20	0	0	0	20	0	0	0
30	0	0	0	30	0	0	0
40	0	0	0	40	0	0	0
50	0	0.010	0.029	50	0	0	0
60	0.01	0.029	0.055	60	0	0	0
70	0.073	0.11	0.16	70	0	0	0
80	0.27	0.34	0.41	80	0.16	0.23	0.31
90	1	1	1	90	1	1	1

The 95% confidence intervals for the cumulative histograms were estimated by using the method for bias-corrected and accelerated (BCa) bootstrap intervals. The number of bootstrap samples for each histogram was 5000.

Supplementary Figure 2

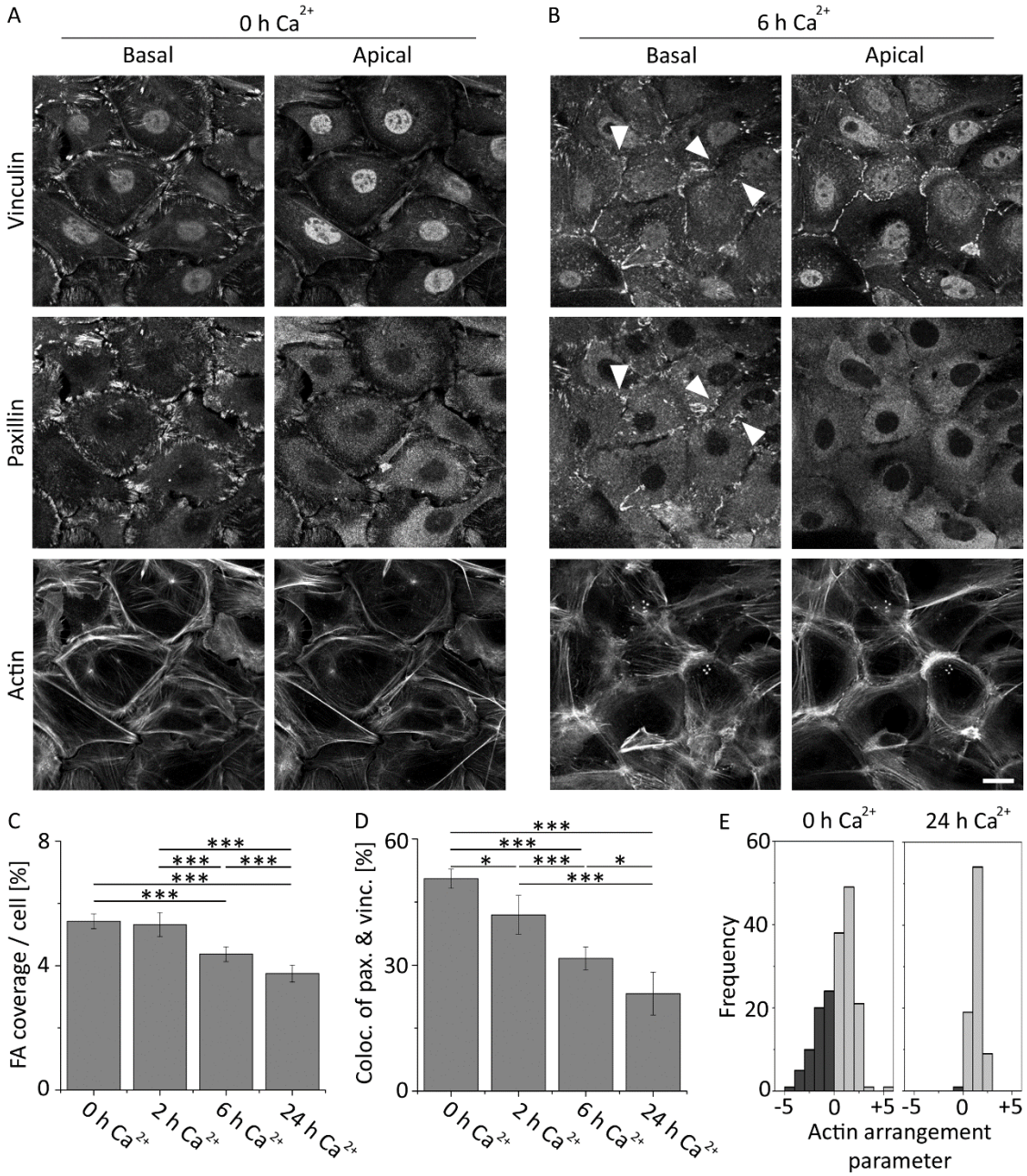

Supplementary Figure 3

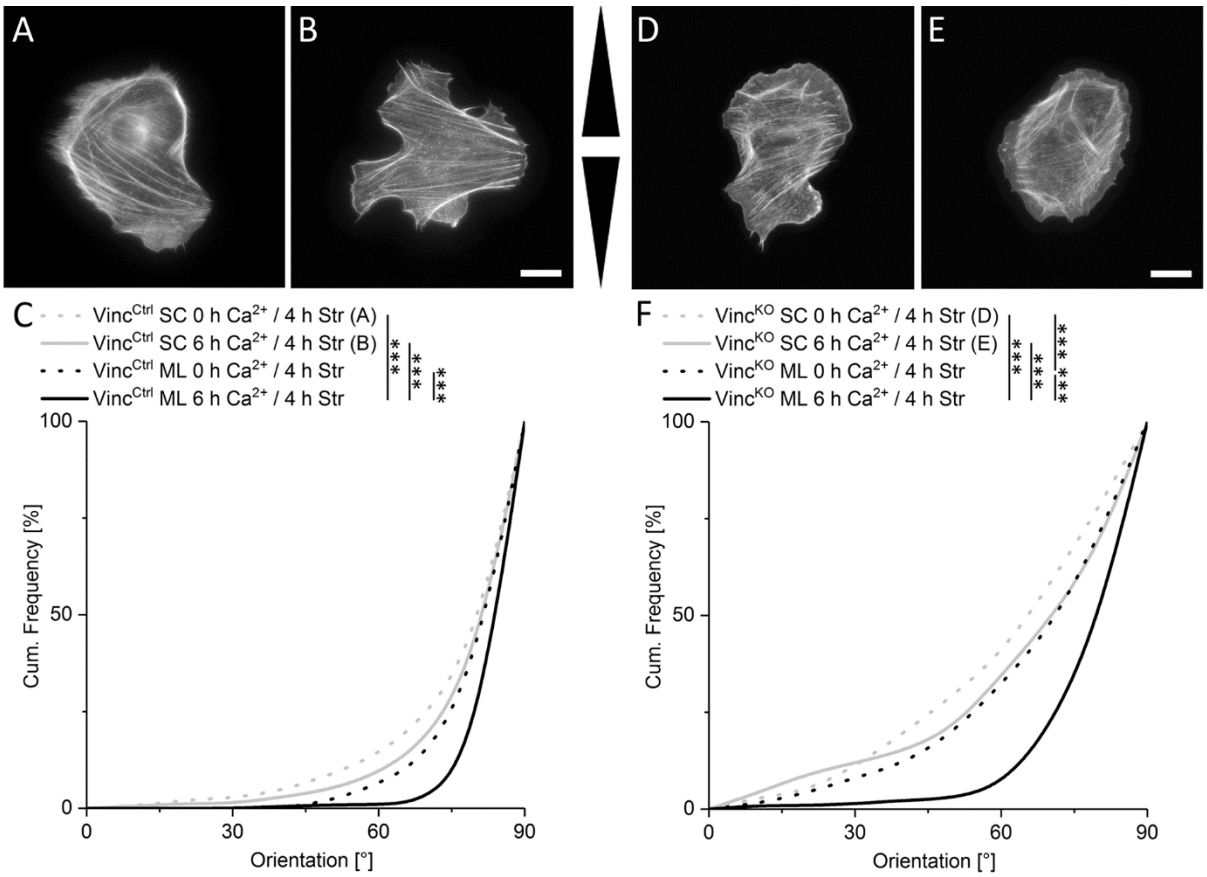

Supplementary Figure 4

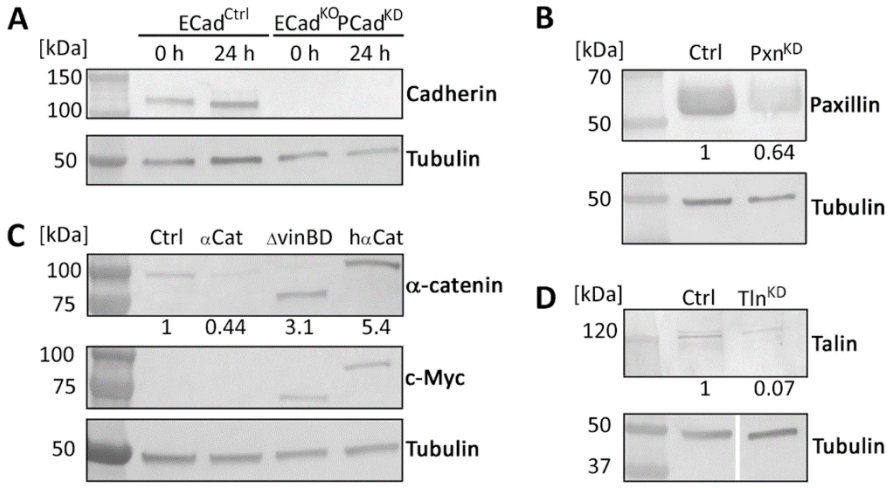

Supplementary Figure 5

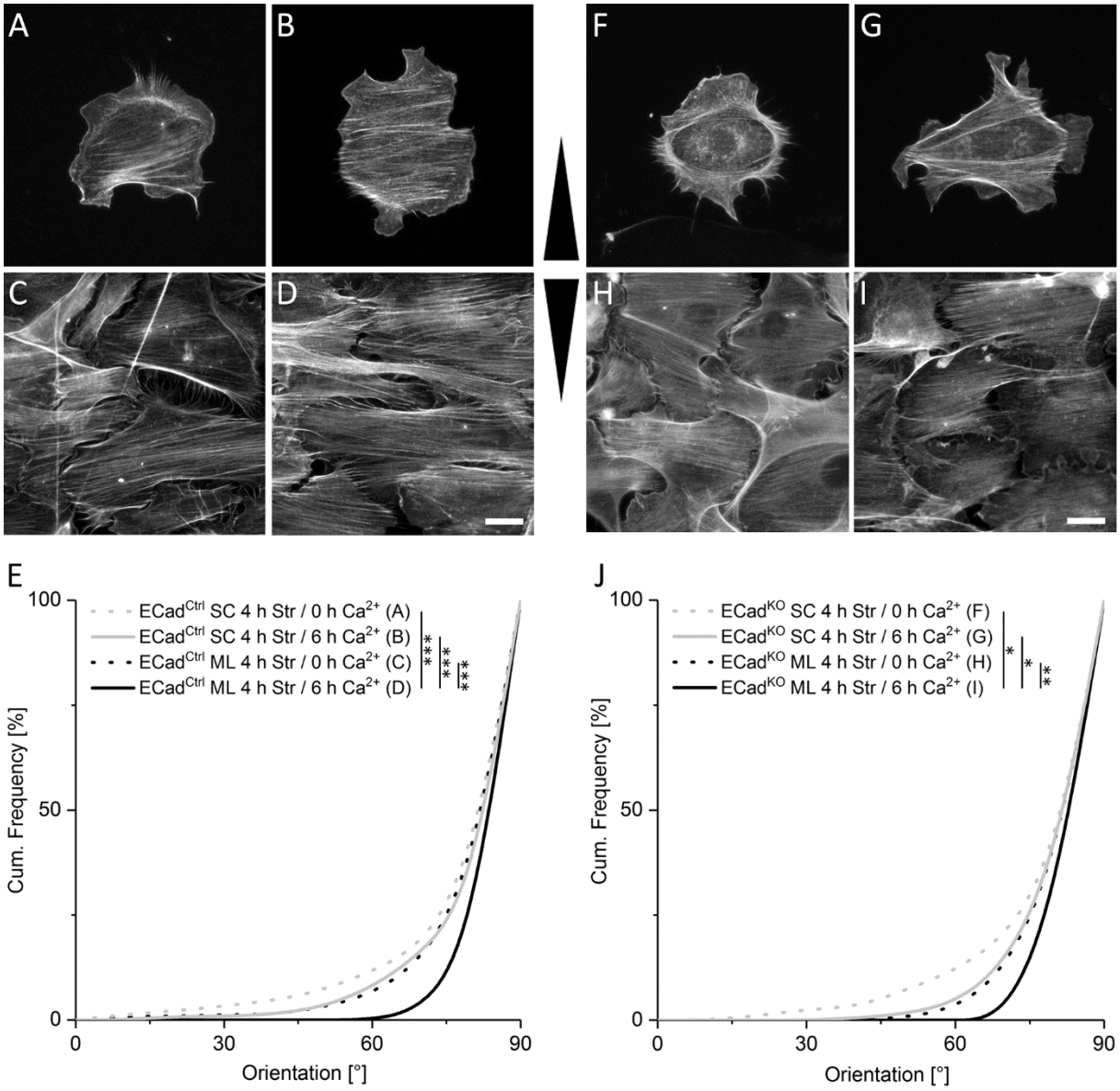

Supplementary Figure 6